Spatial variability of liquid water path in marine low cloud: Part I. Probability distributions and mesoscale cellular scales.

ROBERT WOOD* and DENNIS. L. HARTMANN

University of Washington, Seattle, Washington

October 27, 2003

Abstract

Aspects of the liquid water path (LWP) spatial probability distribution functions (pdf) and power spectra in marine low cloud over the subtropical NE and SE Pacific Ocean are examined using daytime retrievals for two months of data from the Moderate Resolution Imaging Spectroradiometer (MODIS) on the NASA Terra satellite. It is shown that the pdf can be described to a good degree of accuracy using a modified Gamma distribution in accordance with earlier work. The pdf is used to validate and constrain a simple Gaussian physical model of the mesoscale variability that links cloud LWP variability with the underlying boundary layer thermodynamical structure. Importantly, this model couples variability of the cloud LWP with the cloud fraction, and so may be used in large-scale numerical models to account for unresolved variability. Optical depth spatial variability is shown to be well modelled using an adiabatic assumption with constant droplet concentration. A simple formulation for albedo biases is presented that is implemented as a simple reduction in the cloud fraction. Power spectral analysis is used to determine the scale dependence of the LWP pdf. It is found that the majority of power spectra, characteristic scales exist that are related to mesoscale cellular convection (MCC). However, despite the existence of characteristic scales in many cases, it is shown that in the ensemble, the liquid water path exhibits a surprisingly universal scaling with an exponent close to -5/3 over scales up to at least several hundred kilometers.

1. Introduction

Significant spatial variability in low (marine boundary layer, MBL) cloud structure exists on scales of metres to hundreds of kilometres (Cahalan and Snider 1989; Davis et al. 1996; Marshak et al. 1997; Wood and Taylor 2001). Observations show that there is a tendency for boundary layer clouds to self-organize into mesoscale cellular or roll-like structures (see reviews by Agee et al. 1973; Atkinson and Zhang 1996), with dominant horizontal scales much greater than the depth of

* *Corresponding author address:* Dr. Robert Wood, Atmospheric Sciences, University of Washington, Seattle, WA; *e-mail: robwood@atmos.washington.edu.*

the MBL. Mesoscale variability in low cloud needs to be understood because of its importance in determining the mean radiative transfer properties (Cahalan et al. 1994; Barker 1996a,b; Oreopoulos and Davies 1998a,b; Rossow et al. 2002), and in controlling the precipitation rate (Rotstayn 2000; Pincus and Klein 2000; Larson et al. 2001; Wood et al. 2002).

In the marine boundary layer, MCC can be of the open form (containing narrow regions of cloud around the cell edges and broad regions of clearing between) or closed form (broad regions of thick stratiform cloud in the cell centers often with relatively narrow regions of thinning or clearing at the edges). The MCC aspect ratios (cell center separation:BL depth) are typically 3-40 (Atkinson and Zhang 1996), significantly larger than those (usually 2-4) found in BR convection.

Boundary layer roll-type structures and other anisotropic features are more common when the wind speed is quite high (> 10 m s^{-1}) often with a maximum in the BL (Hein and Brown 1988). Rolls can be classified into two types. The first, and simplest type, are those that have a single horizontal scale approximately equal to the BL depth z_i. Aspect ratios (distance between adjacent roll updraughts:z_i) are typically 1-4 for these rolls which tend to form in near neutral conditions. The second type of roll structures contain multiple scales (Walter and Overland 1984), have aspect ratios of 10-20, and are generally associated with convectively driven cloud streets, (Atkinson and Zhang 1996), but can sometimes be considerably larger. In general, the roll axis is typically aligned along the convecting layer shear vector (Kelly 1994; Cox 1996).

Our current understanding of the dynamic and thermodynamic structure of mesoscale BL circulations comes predominantly from *in-situ* observational case studies. Some observations suggest that open-celled MCC is often associated with strong cold advection (sea-air temperature difference > 5 K) and larger total heat flux than closed MCC (e.g. Lenschow and Agee 1974). Critical values of the sensible surface fluxes required for the onset of open-celled MCC suggested by Sheu and Agee (1977) are not supported by later observations (Brummer et al. 1986). Closed MCC are almost always found over water, especially in regions of stratocumulus and stratocumulus to cumulus transition. MCC is the predominant cloud structure for stratocumulus when the boundary layer is deeper than 1 km (Atkinson and Zhang 1996) and is found less often in very shallow stratus-topped boundary layers. It is likely that some form of boundary layer decoupling (Turton and Nicholls 1987; Bretherton and Wyant 1997) is required to allow mesoscale circulations to grow. A qualitative climatology of the prevalence of closed and open MCC over the global oceans was presented by (Agee et al. 1973), showing the tendency of closed cells to form over cold ocean currents and open cells to form over warm ocean currents.

Because it is driven by thermal convection and confined to a thin layer that is quasi-infinite in horizontal extent, attempts have been made to model closed MCC using BR theory (e.g. Agee 1987; Rand 1995). However, none of the attempts have been entirely satisfactory in generating (a) the large aspect ratios; (b) the narrow downdraughts and weak exapansive updraughts that appear to be integral components of these cells (Rothermell and Agee 1980; Moyer and Young 1994). A second theory attempting to account for MCC, mesoscale entrainment instability (Fiedler 1984, 1985) has been shown to require unphysical lower tropospheric structure (Rand and Bretherton 1995) to be of importance in the subtropical MBL. Another notable attempt to explain MCC comes from the work of Shao and Randall (1996), who find that a fully nonlinear model with strong cloud top radiative cooling can produce asymmetric mesoscale cells of the closed MCC type. However, their model tends to produce downdraughts that are considerably stronger (5-10 m s^{-1}) than those typically observed (1 m s^{-1}). In addition, because of the need for broad regions of strong cloud-top radiative cooling, Shao and Randall's model implies that completely different mechanisms must control open and closed cellular convection. Whether this is indeed true remains an open question.

Structure function and singular measures analysis of data from recent field campaigns (Davis et al. 1996; Marshak et al. 1997; Davis et al. 1999), shows that cloud liquid water path exhibits multifractal scaling with inner scales of centimetres and outer horizontal scales that can be tens of km. Scaling exponents are similar to those for Kolmogorov scaling in homogeneous, isotropic turbulence. Although it has not been examined explicitly in most studies, this scaling appears to be one of the characteristic signatures of MCC. Many large-scale numerical cloud schemes use cloud scemes based upon the prediction of the saturation excess pdf, the width of which is determined largely by variability on the mesoscale (e.g. Wood et al. 2002). In these models, the pdf width is often set equal to a fixed value in the lower troposphere. In reality, this pdf width has not yet been adequately constrained by observations nor has its links with MCC been explored. So far, the parameterization of saturation excess pdf width in the boundary layer (e.g. Bechtold et al. 1995; Cuijpers and Bechtold 1995) has implicitly assumed that the thermodynamic variance is dominated by large-eddy scales (~ 1 km). This, clearly, is not the case for most MBL clouds.

There has been considerable debate about the range of scales that exhibit universal scaling in atmospheric systems. Recently, Lovejoy et al. (2001) show that for an ensemble of satellite cloud images there exists a unified scaling with an outer scale of ~ 20000 km. However, it is clear that distinct scales can exist in MCC that violate the scaling locally. We investigate the scale dependence of the LWP power spectrum in this study.

In this paper and its companion we examine aspects of the mesoscale spatial variability in low cloud over the ocean using satellite data. We use liquid water path as our variable of interest as it is directly related to the structural characteristics of the temperature and moisture field. Initially, we look at one point statistics and probability density functions (pdfs), the characteristics of which need to be known in order that both radiative transfer properties and precipitation formation can be accurately predicted. We also examine the scale dependence of the pdf properties using power spectral analysis. In the second part of this study we present a somewhat more quantitative climatology of the occurrence and characteristic of distinct types of mesoscale behavior in the NE and SE Pacific. NCEP/NCAR reanalysis data is used to understand the behavior of the cloud fields in relation to the large scale forcings.

2. Details of MODIS data used

a. Instruments and physical parameter estimation

In this study we use 1 km (at nadir) pixel data from the Moderate Resolution Imaging Spectroradiometer (MODIS), a 24 channel cross-track scanning radiometer. MODIS flies on the NASA Terra polar-orbiting sun-synchronous satellite. Details of the instrument and the are found in King et al. (1992). We use the MODIS Level 2 cloud product's visible/near-infrared algorithm (King et al. 1997) to estimate cloud optical thickness τ and near-cloud top effective radius $r_{e,top}$ resolution for daytime ($\sim$ 10:30 LST) scenes. We choose only to use those data that are within 42° of nadir where the pixel aspect ratios are less than two. This allows us to use data from the central 1030 pixels of the scan. These data are interpolated onto a 1×1 km across- and alon- track grid (1280 km across track).

Estimated uncertainties in retrieved τ and $r_{e,top}$ arise from both physical uncertainties (e.g. sensor calibrations, water vapor or thin cloud above the BL, heavy aerosol layers) and retrieval model uncertainties related to deviations of the true cloud from the model cloud or from variability of optical parameters across the bandwidth of each spectral band. Major sources of error in $r_{e,top}$ are caused by uncertainty in the 2.13 μm central wavelength King et al. (1997), uncertainties in the physical optical constants for water, and uncertainties is the knowledge of atmospheric transmission in the near infrared bands. Overall uncertainty in retrieved $r_{e,top}$ is estimated to be less than 1.5-3 μm.

Nakajima and King (1990) estimate errors in τ caused by errors in the measured reflectance function and suggest that these are typically positively correlated with errors in $r_{e,top}$, so that a $\pm$25% error in τ is found for a $\pm$50% error in $r_{e,top}$. For effective radii commonly found at the top of MBL clouds the errors in τ range from approximately 15% ($r_{e,top} = 10\mu$m) to 7% ($r_{e,top} = 20\mu$m) given errors of 3 μm in effective radius.

Calculation of liquid water path LWP from the $r_{e,top}$ and τ requires a model of the cloud vertical structure. Often, the cloud is modelled as having constant liquid water content and $r_{e,top}$ in the vertical (e.g. Han et al. 1994) which gives $LWP = \frac{2}{3}\rho_w \tau r_{e,top}$. However, most observations of boundary layer clouds indicate that the liquid water content is an approximately linear function of height above cloud base, and that the droplet concentration is approximately constant with height (e.g. Nicholls and Leighton 1986; Brenguier et al. 2000). This leads to an r_e which increases as roughly the cube root of the height above cloud base. This model results in a relationship $LWP = \frac{5}{9}\rho_w \tau r_{e,top}$, giving LWP values a factor of 5/6=0.833 times those using the constant LWC, r_e model. We prefer this model because it accounts for a more realistic representation of the cloud vertical structure.

To estimate errors in LWP derived from MODIS observations we start with the assumption that the errors in τ and $r_{e,top}$ are correlated as is the suggestion from simulations of Nakajima and King (1990), who also find that the absolute error in $r_{e,top}$ is around 1.5 μm at $r_{e,top} = 5\mu$m increasing approximately linearly to 3 μm at $r_{e,top} = 25\mu$m. The fractional error in τ is approximately half that in $r_{e,top}$, so $\Delta\tau/\tau$=0.5$\Delta r_{e,top}/r_{e,top}$. The errors in liquid water path are 45%, 28%, 23%, 20%, 18% for effective radii of 5, 10, 15, 20 and 25 μm respectively.

b. Analysis regions, scenes and acceptance criteria

We are interested here in the structural properties of low (warm) clouds. Our basic unit of analysis is a "scene", a 256×256 (km)^2 portion of the MODIS data. Liquid water path power spectra taken from regions larger than this tend to show a spectral gap at scales of 20-200 km. This spectral gap occurs at considerably larger scales than the classic spectral gap (see e.g. Van der Hoven 1957; Stull 1988). This classic gap separates mesoscale α, β motions from microscale turbulence, whereas for oceanic low cloud fields the spectral gap often falls within the region between the α and β mesoscales.

We select scenes that contain only warm cloud using the MODIS thermal IR cloud top temperature (Ma et al. 2000). We include only wholly oceanic scenes. Some scenes are rejected because of clear instrumental or calibration errors resulting in unphysically large τ. The occurrence of such scenes is most likely uncorrelated with cloud characteristics and so should not bias climatological analyses.

We choose two regions of the East Pacific that are dominated by low cloud for this study (see Table 1). All data are from September/October 2000. Figure 1 shows the regions, together with contours that give the fraction of MODIS scenes that contain no cold cloud, and are therefore accepted for analysis. The ISCCP Rossow and Schiffer (1991) 16 year climatological mid+high cloud amount for September/October (assuming random overlap) is also shown. Over much of the two regions, particularly in the SE Pacific, the mid+high cloud amount is less than 10-15% and the fraction of MODIS scenes analysed exceeds 50%, demonstrating the prevalence of low cloud, and the absence of high clouds to the east of the subtropical gyres. This fraction decreases both equatorward, due to the presence of clouds associated with deep convection, and towards the mid-latitudes, where deep frontal clouds are prevalent. We suspect that the peak in ISCCP mid+high level cloud centered on [80W, 20S] is caused by misclassification of low cloud as mid-level cloud (we reject very few MODIS scenes in this region), a possible artifact related to the strongly capped deep boundary layers close to the SE American coast. ISCCP uses cloud top temperature to estimate the cloud top pressure from NOAA archived profiles of atmospheric temperature derived from TOVS (Rossow and Schiffer 1991). Radiosonde ascents from EPIC 2001 (Bretherton et al. 2003) at [85W, 20S] indicate that the temperature at around 600-700 hPa is approximately the same as the MBL cloud top temperature in this region, leading to a possible misdiagnosis of the height of clouds, especially considering that the TOVS soundings have poor vertical resolution.

c. Scene analysis methods

This study is concerned with the spatial variability of cloud liquid water path and its dependence upon spatial scale. Our goal is to obtain information about the characteristics of cloud structural organization and the variance-containing scales. To this end we use (a) one-point statistics (probability density functions) to examine the types of pdf that exist in boundary layer cloud, and (b) power spectral analysis to examine variance as a function of spatial scale.

Because our analysis involves Fourier methods, we allow overlapping of scenes by 128 km to approximately restore the degrees of freedom lost through data windowing (Welch window). The useful data in each MODIS granule (1280 km across swath by 2030 or 2040 along swath) is divided into 9×15 overlapping 256×256 km scenes. Each scene is screened for the presence of cold cloud and erroneous data before being passed to the analysis routines.

3. Liquid water path probability density functions (pdfs)

a. Forms and models for LWP pdf

If a suitable analytical probability density function (pdf) can be found to describe variations in liquid water path within a grid box then it is possible to define the moments as simple functions of a small number of controlling parameters. Such an analytical pdf can provide a framework for characterisation of cloud variability and will be useful in the parameterisation of cloud inhomogeneity for large-scale numerical models. Oreopoulos and Davies (1998b) examine distributions of τ from AVHRR satellite data, fitting them using gamma, beta and lognormal distributions. They conclude that the gamma distribution gives the poorest fit for purposes of correcting albedo biases. However, they do suggest that in many cases the poor fit is a result of a small number of very large τ values which distort the variance, leading to poor fits. These are most likely from datasets which did not exclusively comprise low-level clouds. Better agreement is obtained when a maximum likelihood estimator, rather than the method of moments, is used to define the parameters of the gamma pdf. The gamma distribution was used to characterise τ distributions in boundary layer clouds (Barker 1996b; Oreopoulos and Davies 1998a) and performed as well as the lognormal distribution. Of course, the choice of a pdf form depends upon its purpose. When calculating albedo bias corrections, it is important to use a pdf that produces accurate low (between 0th and 1st order) moments, because albedo-τ curves are concave. Deriving non-linear process rates which depend upon a parameter, such as LWP, to a high power, clearly requires accurate prediction of high order moments. It is therefore necessary to test the chosen pdf form using the observed distributions to determine its suitability. It is preferable if a single functional form can be used to estimate both the sub-unity and the higher moments.

In this study we concentrate on four distribution forms, described below, to model the liquid water path pdf (see Table 3).

The form of the gamma ($P_\Gamma(x)$) and lognormal ($P_{LN}(x)$) distributions are given by

$$P_\Gamma(x) = \frac{1}{\Gamma(\gamma_x)} \left(\frac{\gamma_x}{\overline{x}}\right)^{\gamma_x} x^{\gamma_x - 1} \text{exp}\left(-\frac{\gamma_x x}{\overline{x}}\right) \tag{1}$$

and

$$P_{LN}(x) = \frac{1}{sx\sqrt{2\pi}} \text{exp}\left[-\frac{(\ln x - \mu)^2}{2s^2}\right] \tag{2}$$

where $\overline{x}$ and σ_x are the mean and standard deviation of x, $\gamma_x = (\overline{x}/\sigma_x)^2$, $\mu = \overline{\ln x}$, and $s = \sigma_{\ln x}$. For the LN distribution, μ and s are analytically related to $\overline{x}$ and σ_x. Thus, both $P_\Gamma(x)$ and $P_{LN}(x)$ are two-parameter distributions, with the two parameters obtainable from observed pdfs. However, there are two options for obtaining the parameters $\overline{x}$ and γ_x for the Γ distribution from the observed pdf. The two methods are the method of moments and the maximum likelihood estimaton (MLE). The first uses the observed mean $\overline{x_{obs}}$ and standard deviation $\sigma_{x,obs}$ (i.e. moments of order 1 and 2) of x to calculate γ_x directly. The MLE method uses $\overline{x_{obs}}$ and $\overline{\ln(x_{obs})}$, also calculable from the pdf of x, to estimate γ_x (e.g. Oreopoulos and Davies 1998b):

$$\gamma_{MLE} = \frac{1 + \sqrt{1 + 4(\ln \overline{x} - \overline{\ln x_{obs}})/3}}{4(\ln \overline{x} - \overline{\ln x_{obs}})} \tag{3}$$

The MLE method is less sensitive to the high x tail of the distribution than is the method of moments. We examine the consequences of this in Section **3.**b.

The last two pdfs result from physical models that link LWP variability with variability in other physical parameters. Such linkages may prove to be useful for the goal of physical parameterization. The Gaussian cloud thickness model (Gaussian-h model) is presented in Considine et al. (1997) and expanded upon in Jeffery and Austin (2003), and is found to be relatively successful at describing LWP variability in unbroken stratocumulus (Wood and Taylor 2001). Its applicability to broken clouds is not known, although there is evidence to indicate its potential utility in modeling broken MBL cloud **?**. The potential advantage of this type of model is that it can be used to link the variability in the cloud LWP within a region with variances in boundary layer thermodynamic variables (temperature, moisture) which may be estimated in a large-scale numerical model. Further, as will be shown, the model LWP variability, when expressed using the parameter $\gamma_{LWP} = (\overline{LWP}/\sigma_{LWP})^2$ is related to the area cloud fraction CF using a single scale-independent function.

The Gaussian-h model results in a LWP pdf, for the cloudy fraction CF of the region, that is a function of two inputs: the mean $\overline{h}$ and standard deviation σ_h of the distance h between the cloud top (inversion) and base (LCL):

$$P_{\text{Gaussian}-h} = \frac{1}{CF\,\Gamma_{ad} h\sqrt{2\pi}} \exp\left\{-\frac{(h-\overline{h})^2}{2\sigma_h^2}\right\} \quad (h > 0) \tag{4}$$

where

$$CF = \frac{1}{2}\left\{1 + \text{erf}(\overline{h}/\sqrt{2}\sigma_h)\right\}. \tag{5}$$

Note that values of $h < 0$ indicate that the LCL is above the inversion and so no cloud is present. Only a weak dependence upon atmospheric pressure and temperature exists (through variations in Γ_{ad}, the adiabatic height gradient in liquid water content) within subtropical regions.

A 1:1 mapping exists between the coordinate system $[LWP, \gamma_{LWP}]$ and $[\overline{h}, \sigma_h]$ that we investigate further in Part II of this study.

The saturation excess Gaussian pdf is also used to obtain a liquid water path pdf. To obtain the LWP pdf from this we make the assumption that $\overline{q_t} - q_{sat}(\overline{T_l}, p)$ increases linearly with height, where q_t is the total water content and q_{sat} is the saturation specific humidity. The liquid temperature T_l is defined as $T_l = T - L_v q_l / c_p$, where q_l is the liquid water content, and L_v and c_p are the specific heat of condensation of water and the specific heat capacity of air respectively. In a boundary layer that is columnwise adiabatic, T_l decreases linearly with height, and q_t is constant with height, leading to a near-linear increase in saturation excess with height for clouds of small vertical extent. Maximum overlap of clouds is assumed and the pdf width is assumed constant in any given scene at all levels in cloud.

The Gaussian-s model is used in this study in conjunction with MODIS observed LWP pdfs to derive estimates of the saturation excess pdf width σ_s, with s defined as

$$s = aq_t' - b\theta_l' + c \tag{6}$$

where

$$a = \left\{1 + \frac{L_v}{c_p}\left(\frac{\partial q_{sat}}{\partial T}\right)_{T=T_l}\right\}^{-1}, \tag{7}$$

$$b = a\frac{\overline{T}}{\overline{\theta}}\left(\frac{\partial q_{sat}}{\partial T}\right)_{T=T_l}, \tag{8}$$

$$c = a(\overline{q_t} - q_{sat}(\overline{T_l}, p)). \tag{9}$$

Conceptually one can think of the LWP pdf as a reflection of the underlying boundary layer saturation excess pdf. For zero cloud top fluctuations, the Gaussian-h model and the Gaussian-s models are equivalent. Even without this assumption, the forms of the LWP pdfs are the same for the two models; zero cloud top fluctuations allows equivalence between h and s, so that a 1:1 mapping exists between $[LWP, \gamma_{LWP}]$ and $[\overline{s_i}, \sigma_s]$, where s_i is the saturation excess at the inversion base. The variables h and s are linearly related because boundary layer clouds are thin enough that the adiabatic liquid water content (or, equivalently, s) increases linearly with height. We can then write relationships between the h and s means and variances:

$$\overline{s_i} = \Gamma_{ad}\overline{h}; \quad (10)$$

$$\sigma_s = \Gamma_{ad}\sigma_h. \quad (11)$$

For the temperature and pressure range of the clouds observed in the NE and SE Pacific, the 5th, 50th and 95th percentiles of Γ_{ad} are 1.66, 1.92 and 2.13 g kg^{-1} km^{-1} respectively.

b. Observational validation

For the pdf forms described above, we use MODIS data to estimate their suitability for representing LWP spatial variability. To demonstrate the range of observed and modelled distributions of LWP we use four test scenes (each 256×256 (km)^2) containing a range of boundary layer cloud types and structures (Fig. 2). Scene (a) contains relatively featureless stratus cloud quite close to the coast of California and is fairly typical of the clouds found in this region throughout the year. Scene (b) contains relatively unbroken stratocumulus cloud with small mesoscale convective cells. This cloud is typical of the extensive stratocumulus sheets over the oceans to the west of continents. Scene (c) contains large stratocumulus cells with cumulus patches below typical of the transition regions in the trade wind boundary layers. There are breaks towards the edges of the cells, possibly due to the absence of cumulus convection to feed the overlying stratiform cloud deck with moisture (Klein et al. 1995). Scene (d) contains open-celled convective clouds. The four scenes together are representative of the range of boundary layer cloud types found in the subtropics. Dates and locations, together with a number of parameters obtained for each of these scenes are given in Table 2. The MODIS cloud mask (Ackerman et al. 2002) is used to determine the fraction of cloudy pixels, i.e. CF. The characteristic lengthscales are defined in Section **4.**a.). Also shown are values of γ_{LWP} calculated directly from the data and using the MLE method. The LWP skewness S_{LWP} is also shown. This increases considerably as the clouds become more heterogeneous and there is a tight coupling between γ_{LWP} and skewness

The LWP pdfs for the four test scenes are shown in Fig. 3(a,b). Although the LN distribution appears to be a better match to observations at low values of LWP for scenes (c) and (d), the LN is too broad at high LWP. In all cases, observed tails are narrower than those from the LN model, and match better with those from the Γ distribution. Liquid water path observations become very unreliable for $LWP < 10$ g m^{-2} and the pdfs often become more noisy and unreliable at these values. Figure 4 shows the observed and model pdf relationships between the second order moments and higher moments (skewness S and kurtosis K). MODIS data are presented as contours of the 2D joint distribution. Each model pdf form has a different but unique relationship between these moments. Both the Γ and the Gaussian-h pdfs represent the observations fairly well. The LN pdf overestimates skewness and kurtosis for any given value of γ_{LWP}. This would result in considerable overprediction of the rates of processes, such as autoconversion rate, that are strongly affected by higher moments (e.g. Wood et al. 2002).

Figures 5 and 6 show cumulative contribution to the moments of order 0.5 and 3 respectively as a function of LWP. For moment order 0.5, all models perform well. For higher moments the LN distribution tends to overestimate the moments, especially in the more heterogeneous cases (images (c) and (d)). Both the Γ pdfs perform well for $\gamma > 1$. For the more heterogeneous cloud cases the method of moments results in more accurate higher order moments. This is expected because the method of moments generates the pdf based upon the observed values of the first and second moments, whereas the MLE method does not rely on the second moment. Both the Gaussian-h and Gaussian-s models reproduce the higher order moments well.

The overestimation of higher order moments by the LN distribution is a general result, and is most severe (a) for more heterogeneous LWP fields; (b) for higher order moments. The other pdf forms considered provide quite realistic relations between the different moments of the LWP distribution, as demonstrated in Fig. 4. It is concluded that the Γ pdf predicted using the method of moments provides a suitable description of the LWP pdf in marine boundary layer cloud, and estimates moments of the pdf with a good degree of reliability and small overall bias.

For the Gaussian-h and Gaussian-s distributions, there is a single unique relationship between γ_{LWP} and the cloud fraction CF. An analytic form for the relationship is possible, but is unwieldy. Figure 7 shows the relationship between cloud fraction CF and γ_{LWP} for all the SE Pacific MODIS scenes. The NE Pacific data (not shown) are very similar. Although both observations and models exhibit a similar behavior, with γ_{LWP} increasing as CF approaches unity, in almost all cases the observed values of γ_{LWP} are greater (i.e. the LWP fields are less variable) than both the model values at a particular CF. The Gaussian curve appears to form the lower limit of the observations. This is somewhat surprising given that Wood et al. (2002) find that aircraft-derived CF is well modeled as a function of $\overline{s}/\sigma_s$. Possible explanations for the lower LWP variability in the observed fields for a given cloud fraction are (a) that, in general, any one scene does not contain a single statistical regime and that this degree of statistical nonstationarity results in changes to the $CF - \gamma_{LWP}$ relationship; (b) that the observed fields tend to have larger values of γ_{LWP} because cloudy pixels with low LWP values are categorized as clear sky. It is clear that this always results in observed CF and γ_{LWP} values that are too low and too high respectively, but it is not clear what the magnitude of this effect is.

To assess (a) above, we obtain a quantitative measure of the stationarity in the MODIS scenes using (i) the degree to which a plane surface fit removed from the LWP field reduces its variance, and (ii) the reduction in variance that is obtained when applying the Welch window. For scenes with stationary statistics, the surface fit should only have a minimal effect upon the variance, and the Welch window should reduce the scene variance by a factor of 225/64=3.52. We choose those scenes for which the surface fit removal reduces the variance by less than 10% (37% of scenes) *and* the Welch window reduces the variance by a factor of 3.02-4.02 (35% of scenes), giving a total of 1377 "stationary" scenes for the NE Pacific data. We also find the least "stationary" scenes (1602 scenes) by selecting those scenes for which the surface fit removal reduces the variance by more than 15% (31% of scenes) *and* the Welch window reduces the variance by less than a factor 2.77 or more than a factor 4.27 (51% of scenes). We examine the $CF-\gamma_{LWP}$ relationship for both sets of scenes by binning as a function of CF (Fig. 8). For all CF the stationary scenes tend to have smaller γ_{LWP} than the least stationary scenes. The difference in γ_{LWP} between the most and least stationary scenes is most marked for $0.6 < CF < 0.9$, but the most stationary scenes still have LWP fields that remain considerably more homogeneous than the corresponding Gaussian models. This indicates that the mixing of statistically distinct regimes (as in the least stationary scenes), is not the sole factor.

The thresholding issue (b) above is addressed by deriving CF and γ_{LWP} only for LWP values greater than some threshold value LWP_{thresh}. We do the same for the Gaussian-h and Gaussian-s models. A reasonable value of LWP_{thresh} is 5 g m^{-2}, as this corresponds to $\tau \sim 1$ (for $r_e = 10\mu$m, typical for marine BL cloud). This is close to the observational error in the MODIS-observed τ

(see Section **2.**a.). For the thresholded data, CF values are smaller (median reduction 0.013) and γ_{LWP} values generally higher (median increase 0.047). This does not represent a particularly large change. However, when we apply the same thresholding to the Gaussian pdfs, we find marked differences that bring the observations and model results into closer agreement (Fig. 9). We conclude that much of the disagreement between measured and modeled $CF - \gamma_{LWP}$ in Fig. 7 is due to differences in the observed and modeled distributions for $LWP < 5$ g m^{-2}. While there may be some real differences at these low values of LWP, the measurement uncertainties preclude further investigation.

c. Relationship between LWP and τ variability

Optical thickness spatial variability is strongly related to that in LWP, but the exact relationship depends upon the ratio of the variability in the droplet concentration (or cloud-top effective radius) to that in the LWP, and upon the degree of correlation between these two fields (Sczodrak et al. 2002). Considering the case where the cloud droplet concentration N_d has no mesoscale or height variability, for an adiabatic cloud, local τ is proportional to $LWP^{5/6}$. With this simple linear transform, for the Γ distribution of LWP,

$$\gamma_\tau = \left(\frac{6}{5}\right)^2 \gamma_{LWP} = 1.44\gamma_{LWP} \tag{12}$$

where $\gamma_\tau = (\overline{LWP}/\sigma_{LWP})^2$. For the special case where the liquid water path and $r_{e,top}$ are completely uncorrelated, one finds

$$\gamma_\tau = \left(\gamma_{LWP}^{-1} + \gamma_{re}^{-1}\right)^{-1} \tag{13}$$

Figure 10 shows that in general, the observed τ fields are less variable than the LWP fields ($\gamma_\tau > \gamma_{LWP}$), because positive correlations usually exist between LWP and $r_{e,top}$. This behavior is expected for an adiabatic cloud with a droplet concentration that is only weakly variable (Eqn. 12). The inset shows that $r_{e,top}$ fields are much less variable than the LWP fields (5th and 95th percentiles of $\gamma_{r_e}/\gamma_{LWP}$ are 2.5 and 12.4 respectively). The shaded regions in Fig. 10 show the range of values of γ_{LWP} and γ_τ for uncorrelated LWP and $r_{e,top}$ (darker shading) and for uncorrelated LWP and N_d (lighter shading), indicating that the observed γ_τ-γ_{LWP} relationship is most consistent with an model in which LWP and N_d are uncorrelated and the mesoscale variability of droplet concentration is quite weak ($\gamma_{N_d}/\gamma_{LWP}$ is approximately lognormally distributed with 5th and 95th percentiles equal to 1.7 and 32.5).

d. Albedo biases

Radiative properties of inhomogeneous clouds depend upon both the mean and the variability of τ (Cahalan et al. 1994; Oreopoulos and Davies 1998a). Cloud inhomogeneity decreases albedo for the same $\overline{\tau}$ because local albedo A is a concave function of local τ for all solar zenith angles. The mean albedo $\overline{A}$ of a region is therefore dependent upon CF, the clear sky albedo A_{CLR}, and the pdf of τ in the cloudy fraction of the region. There have been a number of attempts to quantify the magnitude of the albedo error (the "albedo bias") that arises when spatial variability is ignored. The estimates of Cahalan et al. (1994) probably overestimated the errors because an overly broad pdf of liquid water path taken over several days of observations was assumed. This demonstrates that the degree of albedo bias increases as the time-space scales increase (Oreopoulos and Davies 1998a). Here, our 256×256 km regions are similar in size to a GCM grid-box. To assess the magnitude of the albedo errors, we ask the question *what reduction in cloud fraction is required to obtain the correct mean albedo while treating the cloudy portion of the domain as a homogeneous cloud having the same $\overline{\tau}$ (as the observed heterogeneous cloud)?*.

Some simple manipulation leads to a reduction ΔCF in cloud fraction CF, where

$$\Delta CF = CF \frac{A(\overline{\tau}, \theta) - \overline{A(\tau, \theta)}}{A(\overline{\tau}, \theta) - A_{CLR}}. \tag{14}$$

Here, $A(\overline{\tau, \theta})$ is the albedo of the cloudy fraction calculated using the mean τ (i.e. the homogeneous cloud albedo), and $\overline{A(\tau, \theta)}$ is the albedo of the heterogeneous cloud scene. Here, we consider only the albedo of the boundary layer. We find from radiative transfer calculations using the Fu-Liou scheme (Fu and Liou 1992) that values A_{CLR}=0.04-0.06 are common for subtropical and lower midlatitude boundary layers and zenith angles $< 60°$. Here, we assume a constant value $A_{CLR} = 0.05$. The results are quite insensitive to the precise choice.

One advantage of the ΔCF measure is that it is almost insensitive to the solar zenith angle θ. Figure 11 shows ΔCF as a function of CF for all the NE Pacific scenes. Because the cloud homogeneity and cloud fraction are quite tightly coupled, there is a tight relationship between ΔCF and CF. For $CF < 0.8$, ΔCF increases approximately linearly with CF because cloud LWP variability (γ_{LWP}) is not a strong function of CF (Section **3**.b.). At larger CF, ΔCF reduces because clouds rapidly become more internally homogeneous (γ_{LWP} increases rapidly with CF). The results are almost independent of the (assumed) solar zenith angle. The cloud fraction reduction is almost always less than 0.2, suggesting that while cloud inhomogeneity is a significant modulator of mean albedo, the effects are often quite small for boundary layer clouds. It is possible to use this relationship as the basis for a parameterization of the radiative transfer for inhomogeneous boundary layer clouds. The reduced cloud fraction $CF - \Delta CF$ could be used in a radiative transfer scheme to account for unresolved variability.

4. Scale dependence of the pdf

Increases in climate and NWP model resolution are expected over the coming years, yet little attention has been paid to the scale dependency of cloud and boundary layer process parameterizations. For example, many cloud schemes in these models use pdf formulations to describe the subgrid variability in thermodynamics and hence clouds. However, until the paper by Cusack et al. (1999), little attempt has been made to treat the pdf widths as scale dependent parameters in large-scale numerical models. Power spectral and/or structure function analysis reveals that pdf widths of a range of cloud parameters increase as the scale increases (e.g. LWP, Cahalan and Snider (1989); liquid water content, Davis et al. (1996); cloud base height, Wood and Taylor (2001); drizzle precipitation rate, Wood (2003)). Cusack et al. (1999) applies a 5/3 scaling exponent to parameterize subgridscale variability of the small scales (< 60 km) based upon the resolved scales (variance of a 3×3 grid resolution 60 km). There is some evidence of a universal scaling of cloud properties over this range (Lovejoy 1982), but the compositing of a large number of different cloud scenes and regimes to form a single scaling function may miss features that interfere with the simple power law scaling. We examine the scaling using MODIS data in the following two subsections.

a. Power spectra and characteristic lengthscales

For each MODIS scene we derive the 2D power spectrum as a function of total wavenumber k, where $k^2 = k_x^2 + k_y^2$ and k_x, k_y are the wavenumbers along the axes of the square scene. The image is detrended by removing the best-fit plane and then windoed using a Welch two dimensional window, before application of the FFT. Power spectra for the four test scenes are shown in Fig. 12. The spectra are all normalised so that $\int_0^\infty P_{LWP} dk = \sigma^2_{LWP,all}$ where $\sigma_{LWP,all}$ is the standard deviation of LWP (including cloud free regions where $LWP = 0$). We find that spectra for both open and closed MCC usually exhibit a peak at a lengthscale we define as λ_1. Power law scaling is usually found at large k. We define the scale at which the spectrum diverges from the power law as λ_2. For closed cellular convection spectra diverge from the power law at a scale close to the peak scale (i.e. $\lambda_1 \approx \lambda_2$, as in Fig. 12(b) and (c)), but for open cells the divergence from power law behavior occurs at a scale somewhat smaller than the cell-scale (i.e. $\lambda_1 > \lambda_2$, as in Fig. 12(b) and (c)). Visual inspection of many MODIS scenes leads to the conclusion that λ_1 and λ_2 can be interpreted as the approximate cell diameter and typical cloud-size respectively. For closed cells these are approximately the same because the gaps between clouds are quite small. Open cells tend to consist of small clouds that form around the perimeter of a larger cellular structure.

After exhaustive testing we constructed methods to determine automatically the lengthscales λ_1 and λ_2 from the power spectral data. In some cases the power law behavior is either not present or limited to scales similar to the Nyquist frequency (0.5 km^{-1}) and cannot be determined using the MODIS data. In these cases λ_2 is undefined. Similarly, some of the scenes do not contain a peak in the power spectrum other than that introduced artificially by data windowing. In such cases λ_1 is undefined.

Mean LWP power spectra for different ranges of the cell size λ_1 are are shown in Fig. 13. Data are taken from the NE Pacific region only; spectra are almost identical for the SE Pacific data. An approximate $-\frac{5}{3}$ power law scaling of the high wavenumber tail is demonstrated. It is also clear that an increase in cell size is, on average, associated with an increase in LWP variance. We scrutinize further the links between LWP variance and the cell size in Part II of this study.

b. The ensemble picture

We have seen that a characteristic cell lengthscale λ_1 is generally found in the LWP power spectrum. This might lead one to the conclusion that this proves a violation in the $\beta-$ and $\gamma-$mesoscale of the universal scaling relations found by Lovejoy (1982). While this does indeed show that local departures from any universal scaling law do exist, it is not clear from the analysis in Section **4.**a. whether or not a universal scaling law exists in an ensemble sense. To investigate this we generate realizations, using an inverse FFT fractal model (Peitgen and Saupe 1988), of liquid water path superscenes that exhbit power law scaling (with exponent β) from 1-512 km. We then split the 512×512 km region into four 256×256 km scenes. For each of the four scenes we obtain the mean $\overline{x_{i,j}}(i = 0, 1; j = 0, 1)$ and the standard deviation $\sigma_{i,j}(i = 0, 1; j = 0, 1)$ of the LWP for just the cloudy portion. We find the ratio α of the mean of the four standard deviations to the standard deviation of the four means $\alpha = \overline{\sigma_{i,j}}/\sigma_{\overline{x_{i,j}}}$. The process is repeated to build up a distribution of α values from many simulations with different scaling exponents β. The magnitude of α determines the ratio of the power that is in scales smaller than the scene size to the power at scales larger than the scene size, and so can be used to validate the parameterization of Cusack et al. (1999) because the above approach can be carried out with groups of four adjacent MODIS scenes. We find that α is almost indepdendent of other parameters (mean LWP, cloud fraction) and depends almost exclusively upon β.

Figure 14 shows distributions of α values from the MODIS datasets in the NE and SE Pacific. All MODIS data with cloud fractions larger than 0.1 are included. Also shown is the model distribution for a scaling exponent of $\beta = -5/3$ which matches fairly well with the observations. The inset shows that the MODIS data are consistent with an ensemble scaling exponent close to

-5/3. This result is somewhat surprising in the light of the findings that most individual scenes have a characteristic scale and therefore a scale break. In spite of this, it appears that nature conspires to maintain a universal scaling in the ensemble throughout much of the mesoscale. This suggests that the organization of the scale breaks happens in such a way that maintains a type of universal scaling when examined over long enough timescales and large enough regions. It may therefore be a reasonable approach to base parameterizations of subgridscale variability upon model-resolved variability at larger scales, although there is a lack of a clear physical mechanism to link the mesoscale cellular convection to variability on scales > 100 km.

5. Discussion and conclusions

A number of analytical tools have been applied to kilometer resolution data from the MODIS instrument on Terra to determine characteristics of LWP spatial variability in MBL clouds. Two regions, both dominated by marine low cloud, form the focus of our study. One-point (pdfs) and two-point (power spectra) measures have been used to characterize the spatial variability.

Through examination of the liquid water path mesoscale variability of subtropical MBL clouds, we have demonstrated that a tight link exists between the triad of parameters $\overline{LWP}$, γ_{LWP} and the cloud fraction CF. The cloud fraction is closely related to spatial variability of the LWP of the cloudy region. The findings provide solid observational support for the general philosophical approach to parameterizing the cloud structural properties using a saturation excess probability density function (pdf), as suggested initially by Sommeria and Deardorff (1977) and Mellor (1977). The use of these statistical schemes in large-scale numerical models (e.g. Smith 1990; Tompkins 2002) has met with a substantial amount of criticism, and some of this stems from the unconstrained nature of the underlying saturation excess pdf, particularly the pdf's width that has effectively been used in many large-scale numerical models as a tunable parameter to balance the top-of-atmosphere radiation budgets. The observations presented in this study, provide a new set of constraints upon the pdf width.

In a second study we examine further the spatial variability properties by looking at the preferred directionality of mesoscale features and diagnosing whether the MCC is of the open or closed cellular variety. Climatologies of these properties are presented and the influence of large scale forcings is investigated.

References

Ackerman, S. A., K. Strabala, P. Menzel, R. Frey, C. Moeller, L. Gumley, B. Baum, S. Wetzel Seeman, and H. Zhang: 2002, Discriminating clear-sky from cloud with modis. MODIS Algorithm Theoretical Basis Document MOD35 ATBD-MOD-06, NASA.

Agee, E. M.: 1987, Meso-scale cellular convection over the oceans. *Dyn. Atmos. Ocean.*, **10**, 317–341.

Agee, E. M., T. S. Chen, and K. E. Dowell: 1973, A review of mesoscale cellular convection. *Bull. Amer. Meteorol. Soc.*, **54**, 1004–1012.

Atkinson, B. W. and J. W. Zhang: 1996, Mesoscale shallow convection in the atmosphere. *Rev. Geophys.*, **34**, 403–431.

Barker, H. W.: 1996a, A parameterization for computing grid-averaged solar fluxes for inhomogeneous marine boundary layer clouds. part 1: Methodology and homogeneous biases. *J. Atmos. Sci.*, **53**, 2289–2303.

— 1996b, A parameterization for computing grid-averaged solar fluxes for inhomogeneous marine boundary layer clouds. part 2: Validation using satellite data. *J. Atmos. Sci.*, **53**, 2304–2316.

Bechtold, P., J. W. M. Cuipers, P. Mascart, and P. Trouilhet: 1995, Modeling of trade wind cumuli with a low-order turbulence model: toward a unified description of cu and sc clouds in meteorological models. *J. Atmos. Sci.*, **52**, 455–463.

Brenguier, J. L., P. Y. Chuang, Y. Fouquart, D. W. Johnson, F. Parol, H. Pawlowska, J. Pelon,

L. Schuller, F. Schroder, and J. Snider: 2000, An overview of the ace-2 cloudycolumn closure experiment. *Tellus*, **52B**, 815–827.

Bretherton, C. S., T. Uttal, . Fairall, C. W., . Yuter, S. E., . Weller, R. A., . Baumgardner, D., . Comstock, K., and R. Wood: 2003, The epic 2001 stratocumulus study. *Bull. Am. Meteorol. Soc.*, in review.

Bretherton, C. S. and M. C. Wyant: 1997, Moisture transport, lower-tropospheric stability, and decoupling of cloud-topped boundary layers. *J. Atmos. Sci.*, **54**, 148–167.

Brummer, B., T. Fischer, and S. Zank: 1986, Aircraft observations of open cellular structures during kontur. *Contrib. Atmos. Phys.*, **59**, 162–184.

Cahalan, R. F., W. Ridgway, W. J. Wiscombe, T. L. Bell, and J. B. Snider: 1994, The albedo of fractal stratocumulus clouds. *J. Atmos. Sci.*, **51**, 2434–2455.

Cahalan, R. F. and J. B. Snider: 1989, Marine stratocumulus structure. *Rem. Sens. Environ.*, **28**, 95–107.

Considine, G., J. A. Curry, and B. Wielicki: 1997, Modeling cloud fraction and horizontal variability in marine boundary layer clouds. *J. Geophys. Res.*, **102**, 13517–13525.

Cox, S. E.: 1996, On the onset of thermal convection between poorly conducting horizontal boundaries in the presence of a shear flow. *SIAM J. Appl. Math.*, **56**, 1317–1328.

Cuijpers, J. W. M. and P. Bechtold: 1995, A simple parameterization of cloud water related variables for use in boundary layer models. *J. Atmos. Sci.*, **52**, 2846–2490.

Cusack, S., J. M. Edwards, and R. Kershaw: 1999, Estimating the subgrid variance of saturation, and its parametrization for use in a gcm cloud scheme. *Quart. J. Roy. Meteorol. Soc.*, **12**, 3057–3076.

Davis, A., A. Marshak, H. Gerber, and W. J. Wiscombe: 1999, Horizontal structure of marine boundary layer clouds from cm to km scales. *J. Geophys. Res.*, **104**, 6123–6144.

Davis, A., A. Marshak, W. Wiscombe, and R. Cahahlan: 1996, Scale invariance of liquid water distributions in marine stratocumulus. part 1: Spectral properties and strationarity issues. *J. Atmos. Sci.*, **53**, 1538–1558.

Fiedler, B. H.: 1984, The meso-scale stability of entrainment into cloud-topped mixed layers. *J. Atmos. Sci.*, **41**, 92–101.

— 1985, Mesoscale cellular convection: Is it convection? *Tellus*, **37A**, 163–175.

Fu, Q. and K.-N. Liou: 1992, On the correlated k-distribution method for radiative transfer in nonhomogenous atmospheres. *J. Atmos. Sci.*, **49**, 2139–2156.

Han, Q., W. B. Rossow, and A. A. Lacis: 1994, Near global survey of effective droplet radii in liquid water clouds using isccp data. *J. Clim.*, **7**, 465–497.

Hein, P. F. and R. A. Brown: 1988, Observations of longitudinal roll vortices during arctic cold air outbreaks over open water. *Boundary Layer Meteorol.*, **45**, 177–199.

Jeffery, C. A. and P. H. Austin: 2003, Unified treatment of the thermodynamic and optical variability of unresolved low clouds. *J. Atmos. Sci.*, in press.

Kelly, R. E.: 1994, The onset and development of thermal convection in fully developed shear flows. *Adv. Appl. Mech.*, **31**, 35–112.

King, M. D., Y. Kaufman, W. P. Menzel, and D. Tanré: 1992, Remote sensing of cloud, aerosol, and water vapor properties from the moderate resolution imaging spectroradiometer (modis). *IEEE Trans. Geosci. Rem. Sens.*, **30**, 2–27.

King, M. D., S.-C. Tsay, S. E. Platnick, M. Wang, and K.-N. Liou: 1997, Cloud retrieval algorithms for modis: Optical thickness, effective particle radius, and thermodynamic phase. MODIS Algorithm Theoretical Basis Document ATBD-MOD-05, NASA.

Klein, S. A., D. L. Hartmann, and J. R. Norris: 1995, On the relationships among low-cloud structure, sea surface temperature, and atmospheric circulation in the summertime northeast pacific. *J. Climate*, **8**, 1140–1155.

Larson, V. E., R. Wood, P. R. Field, J.-C. Golaz, T. H. Vonder Haar, and W. R. Cotton: 2001, Systematic biases in the microphysics and thermodynamics of numerical models that ignore subgrid-scale variability. *J. Atmos. Sci.*, **58**, 1117–1128.

Lenschow, D. H. and E. M. Agee: 1974, The air mass transformation experiment (amtex) preliminary results from 1974 and plans for 1975. *Bull. Am. Meteorol. Soc.*, **55**, 1228–1235.

Lovejoy, S. D.: 1982, Area-perimeter relation for rain and cloud areas. *Science*, **216**, 185–187.

Lovejoy, S. D., D. Schertzer, and J. D. Stanway: 2001, Direct evidence of multifractal atmospheric cascades from planetary scales down to 1 km. *Phys. Rev. Lett.*, **86**, 5200–5203.

Ma, X., Z. Wan, C. Moeller, W. Menzel, L. Gumley, and Y. Zhang: 2000, Retrieval of geophysical parameters from moderate resolution imaging spectroradiometer thermal infrared data: evaluation of a two-step physical algorithm. *Appl. Optics*, **39**, 3537–3550.

Marshak, A., A. Davis, W. Wiscombe, and R. Cahalan: 1997, Scale invariance in liquid water distributions in marine stratocumulus. part ii: multifractal properties and intermittency issues. *J. Atmos. Sci.*, **54**, 1423–1444.

Mellor, G. L.: 1977, The Gaussian cloud model relations. *J. Atmos. Sci.*, **34**, 356–358.

Moyer, K. A. and G. S. Young: 1994, Observations of mesoscale cellular convection from the marine stratocumulus phase of fire. *Boundary Layer Meteorol.*, **71**, 109–134.

Nakajima, T. and M. D. King: 1990, Optical thickness and effective particle radius of clouds from reflected solar radiation measurements. part i: Theory. *J. Atmos. Sci.*, **47**, 1878–1893.

Nicholls, S. and J. Leighton: 1986, An observational study of the structure of stratiform cloud sheets: Part i. structure. *Quart. J. Roy. Meteorol. Soc.*, **112**, 431–460.

Oreopoulos, L. and R. Davies: 1998a, Plane parallel albedo biases from satellite observations. part i: Dependence on resolution and other factors. *J. Clim.*, **11**, 919–932.

— 1998b, Plane parallel albedo biases from satellite observations. part ii: Parameterizations for bias removal. *J. Clim.*, **11**, 933–944.

Peitgen, H.-O. and D. Saupe: 1988, *The science of fractal images*. Springer Verlag.

Pincus, R. and S. A. Klein: 2000, Unresolved spatial variability and microphysical process rates in large scale models. *J. Geophys. Res.*, **105**, 27059–27066.

Rand, H. A.: 1995, Mesoscale dynamics of the marine atmospheric boundary layer. *PhD thesis, University of Washington, Seattle, WA, USA*.

Rand, H. A. and C. S. Bretherton: 1995, Relevance of the mesoscale entrainment instability to the marine cloud-topped atmospheric boundary layer. *J. Atmos. Sci.*, **50**, 1152–1158.

Rossow, W. B., C. Delo, and B. Cairns: 2002, Implications of the observed mesoscale variations of clouds for earth's radiation budget. *J. Clim.*, **15**, 557–585.

Rossow, W. B. and R. A. Schiffer: 1991, Isccp cloud data products. *Bull. Am. Meteorol. Soc.*, **72**, 2–20.

Rothermell, J. and E. M. Agee: 1980, Aircraft investigation of mesoscale cellular convection during amtex75. *J. Atmos. Sci.*, **37**, 1027–1040.

Rotstayn, L. D.: 2000, On the "tuning" of autoconversion parameterizations in climate models. *J. Geophys. Res.*, **105**, 15,495–15,507.

Shao, Q. and D. A. Randall: 1996, Closed mesoscale cellular convection driven by cloud-top radiative cooling. *J. Atmos. Sci.*, **53**, 2144–2165.

Sheu, P.-J. and E. M. Agee: 1977, Kinematic analysis and air-sea heat flux associated with mesoscale cellular convection during AMTEX 75. *J. Atmos. Sci.*, **34**, 793–801.

Smith, R. N. B.: 1990, A scheme for predicting layer clouds and their water content in a general circulation model. *Q. J. R. Meteorol. Soc.*, **116**, 435–460.

Sommeria, G. and J. W. Deardorff: 1977, Subgrid-scale condensation in models of nonprecipitating clouds. *J. Atmos. Sci.*, **34**, 344–355.

Stull, R. B.: 1988, *An introduction to boundary layer meteorology*. Kluwer Academic Publishers.

Tompkins, A. M.: 2002, A prognostic parameterization for the subgrid-scale variability of water vapor and clouds in large-scale models and its use to diagnose cloud cover. *J. Atmos. Sci.*, **59**, 1917–1942.

Turton, J. D. and S. Nicholls: 1987, A study of the diurnal variation of stratocumulus using a multiple mixed layer model. *Q. J. R. Meteorol. Soc.*, **113**, 969–1009.

Van der Hoven, I.: 1957, Power spectrum of horizontal wind speed in the frequency range from 0.0007 to 900 cycles per hour. *J. Meteorol.*, **14**, 160–164.

Walter, B. A. and J. E. Overland: 1984, Observations of longitudinal rolls in a near neutral atmosphere. *Mon. Wea. Rev.*, **112**, 200–208.

Wood, R.: 2003, Drizzle in stratocumulus: part i. *J. Atmos. Sci.*, submitted.

Wood, R., P. R. Field, and W. R. Cotton: 2002, Autoconversion rate bias in boundary layer cloud parameterizations. *Atmos. Res.*, **65**, 109–128.

Wood, R. and J. P. Taylor: 2001, Liquid water path variability in unbroken marine stratocumulus. *Quart. J. Roy. Meteorol. Soc.*, **127**, 2635–2662.

Figure Captions

Figure 1: The two regions (NE and SE Pacific) in this study. Contours show fraction of 256×256 km scenes containing only warm cloud ($T_{top} > 273$ K). Grayscale shading shows ISCCP mid+high cloud amount for Sept/Oct 1984-1999.

Figure 2: Example scenes of MODIS liquid water path in boundary layer cloud showing wide variability in cloud structure. Each scene size is 256×256 km at 1 km resolution. Image times and locations are given in Table 2.

Figure 3: (a) Examples of LWP pdfs for the four test scenes shown in Fig. 2. The observed pdf is shown using filled circles. Also shown are the model pdfs for the lognormal (dotted curve) and gamma distributions with parameters estimated from the method of moments (solid curve) and from the MLE (dashed curve).

Figure 3: (b) As for Fig. 3(a) but with logarithmic axes.

Figure 4: Skewness-γ_{LWP} (a) and kurtosis-γ_{LWP} (b) frequency distribution (contours) from all SE Pacific MODIS scenes. Median values of skewness S and kurtosis K for γ_{LWP} intervals are shown (filled circles). Lines show relationships for the model pdfs.

Figure 5: Cumulative contribution to the moment of order 0.5 from LWP values smaller than

those on the abscissa for the four test scenes shown in Fig. 2. Symbols and curves are the same as those in Fig. 3. All curves are normalised with the observed moment for the full distribution. In all cases the model distribution quite accurately simulate the contributions to the moment from the different LWP values. The best agreement is found for the gamma distribution with γ_{MLE}.

Figure 6: As Fig. 5 but for moment order 3. For higher order moments the lognormal distribution is clearly an inadequate model because the contributions from high LWP values (the distribution tail) are too large. The gamma distribution using the method of moments or the MLE both perform well, as do the Gaussian-h and Gaussian-s models.

Figure 7: Cloud fraction-conditional probability contours (shaded) of γ_{LWP} for all the SE Pacific MODIS scenes. The contours represent 5th, 10th, 25th, 75th, 90th and 95th percentiles. Median CF-conditional values of γ_{LWP} are also shown (filled circles) together with the unique relationship for the Gaussian model.

Figure 8: $CF - \gamma_{LWP}$ for the most "stationary" scenes (open circles) and the most "non-stationary" scenes (filled circles). The error bar limits show the 25th and 75th percentiles for each dataset. The Gaussian model curve is denoted by the solid line.

Figure 9: Cloud fraction CF vs γ_{LWP} for SE Pacific MODIS scenes with minimum LWP thresholds of 5 g m^{-2} (solid circles) and zero (open circles). Also shown is the Gaussian model results with $LWP_{thresh} = 5$ g m^{-2} applied. Agreement between observations and models is considerably better for thresholded data. Error bars ($LWP_{thresh} = 5$ g m^{-2} MODIS data) show the

25th and 75th percentiles. Lines in light gray are model curves for non-thresholded LWP, i.e. those in Fig. 7.

Figure 10: Joint probability distribution of τ shape parameter γ_τ and γ_{LWP}. Contours contain 98% of the MODIS scenes; filled circles are median γ_τ as a function of γ_{LWP}. Darker shaded region shows the range of values that would be obtained if there is no correlation between LWP and $r_{e,top}$, and given the observed range of $\gamma_{r_e}/\gamma_{LWP}$ (see inset). Lighter shaded region shows range for zero correlation between LWP and droplet concentration N_d, for observed range of LWP and N_d variability. Dash-dot line shows the relationship for an adiabatic cloud with homogeneous droplet concentration (i.e. $\tau = LWP^{5/6}$) and an assumed Γ distribution for LWP.

Figure 11: Albedo biases expressed as the reduction ΔCF in cloud fraction CF necessary to obtain the same scene-mean albedo when homogeneity is assumed in the cloudy portion of the scene. Shaded regions show the 5th, 10th, 25th, 75th, 90th and 95th percentiles for the spherical albedo. Solid circles denote median values. This function is quite well parameterized as function of cloud fraction because of the tight coupling between cloud fraction and internal liquid water path variability. Also shown are the median values for solar zenith angles $\theta = 0$ (dotted), $\theta = 22.5°$ (dashed) and $\theta = 45°$ (dot-dashed).

Figure 12: Power spectra calculated using 2D-FFT for the four example scenes shown in Fig. 2. The unsmoothed spectra are shown using the solid line. Averaged spectra are shown using filled circles and approximate 95% confidence limits are given by the light dotted line. The filled triangle on the wavenumber axis shows the "mean" wavenumber used to determine the power law

fit to the large k end of the observed spectra (thick dotted line). The two characteristic lengthscales are defined as λ_1, the wavelength of the highest wavenumber peak in the averaged power spectrum. λ_2, the minimum wavenumber at which the 95% confidence limit of the spectrum exceeds the fitted power law. These scales correspond approximately to cellular diameters and cloud-sizes respectively.

Figure 13: Averaged power spectra four different ranges of the characteristic cell lengthscale λ_1. Vertical gray bars indicate extent of λ_1 ranges.

Figure 14: Probability distribution of $\alpha = \overline{\sigma_{i,j}}/\sigma_{\overline{x_{i,j}}}$ for all MODIS NE and SE Pacific 2×2-scene regions containing $> 10\%$ cloud. Solid line shows distribution resulting from simulations with LWP spatial maps generated with an inverse FFT fractal cascade for which the ensemble scaling expondent is specified to be $\beta = -5/3$. Error bars show the 95% confidence limits for the observed distributions. Vertical lines show the median values of α for the observations. Inset shows the median value of α as a function of β showing that the MODIS observations are well modeled (horizontal lines show the median values from observations) by a fractal cascade with a scaling exponent close to -5/3.

Table 1: Details of the regions examined in this study.

Region	Longitude range	Latitude range	Period [mm/dd/yy]	Scenes analyzed [number]
NE Pacific	110-150W	10-50N	08/20/00-10/31/00	7803
SE Pacific	70-120W	30S-10N	09/01/00-10/31/00	12992

Table 2: Characteristics of the four test images shown in Fig. 2. Parameters listed are cloud fraction CF; characteristic scale of the cells λ_1 and of the cloud structures λ_2; mean liquid water path $\overline{LWP}$; the ratio of square of the mean mean to the variance of LWP for cloudy pixels only, calculated directly (γ) and using the MLE method (γ_{MLE}); liquid water path skewness S_{LWP}; Type of cloud formation (open cells O, closed cells C, or homogeneous H); boundary layer depth z_i.

Image	Date	Location [lat,long]	CF	λ_1 [km]	λ_2 [km]	$\overline{LWP}$ [g m^{-2}]	γ	γ_{MLE}	γ_{LN}	S_{LWP}	Type	z_i [m]
(a)	17 Oct 00	36N,125W	0.99	5.4	N/A[1]	58	5.02	3.72	3.10	0.51	H	610
(b)	18 Aug 00	30N,131W	0.88	10.9	10.3	58	3.13	2.97	2.26	1.45	C	760
(c)	18 Aug 00	26N,135W	0.86	38.5	48.2	72	1.35	1.37	0.65	1.38	C	1100
(d)	13 Oct 00	11S,97W	0.32	35.7	10.1	29	1.24	1.40	0.73	1.72	O	1020

Notes: [1] Characteristic scale undetermined.

Table 3: Forms for the liquid water path LWP pdf examined in this study

Name	Description/Refs
Gamma pdf (Γ);	see Barker (1996a)
Lognormal pdf (LN);	see Oreopoulos and Davies (1998a)
Gaussian-h pdf	The LWP pdf that results from the assumption that in the cloud layer thermodynamic profiles are locally moist adiabatic, with a cloud thickness h that is a Gaussian random variable.
Gaussian-s pdf	The LWP pdf resulting from the assumption of a uniform cloud top height and that at each level below this the saturation excess is distributed using a Gaussian form. The saturation excess pdf width is constant with height and the mean increases linearly with height (adiabatic model). Columns are assumed to be vertically coherent, i.e. the local saturation excess increases linearly with height in each column.

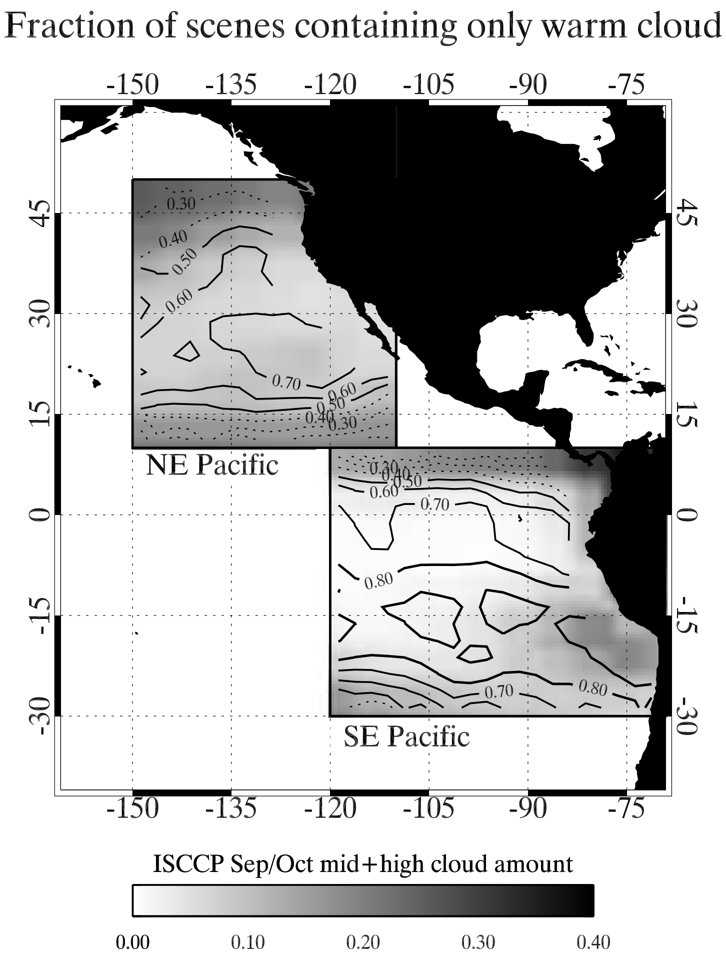
Fraction of scenes containing only warm cloud
-150
-135
-120
-105
-90
-75
45
30
15
0
-15
-30
NE Pacific
SE Pacific
0.30
0.40
0.50
0.60
0.70
0.80
ISCCP Sep/Oct mid+high cloud amount
0.00
0.10
0.20
0.30
0.40

Figure 1:

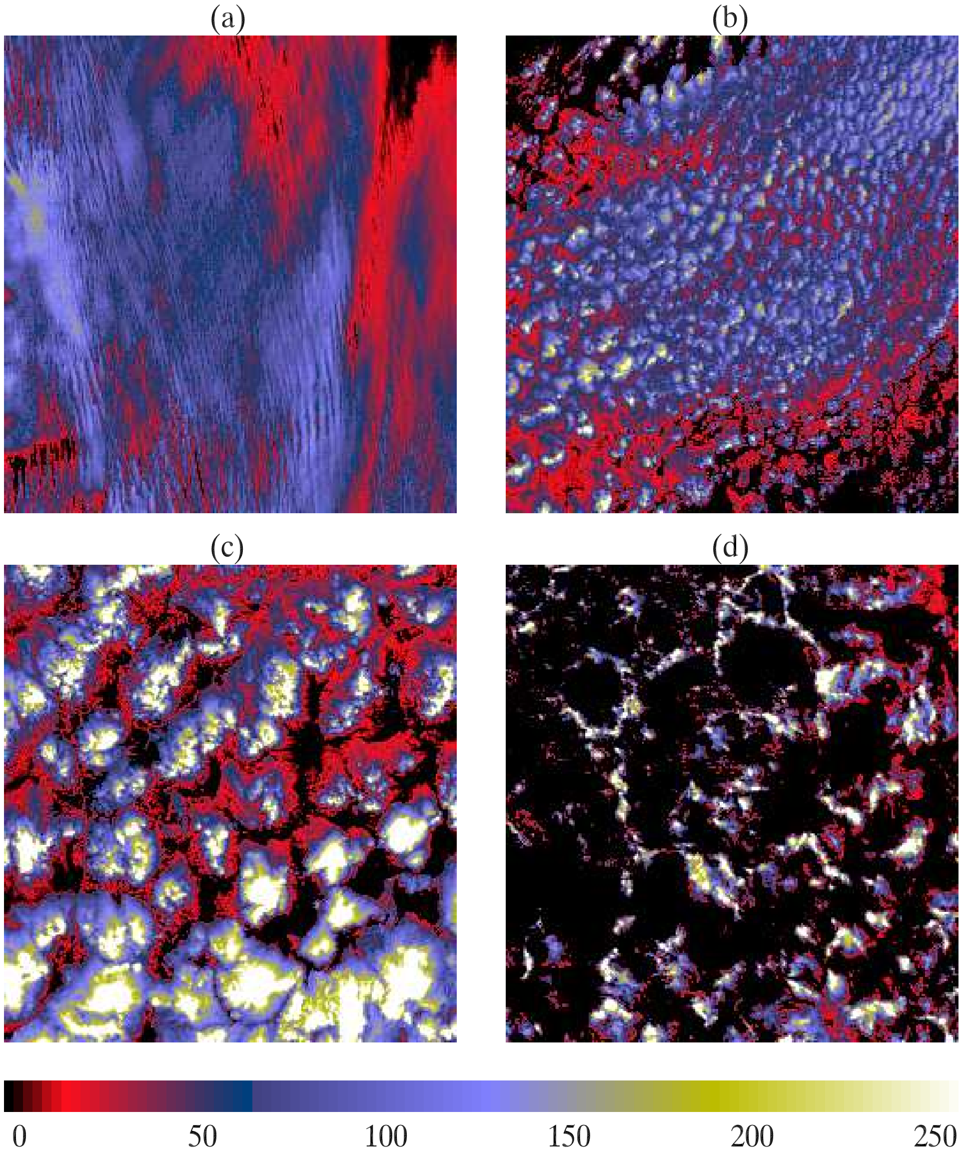

Figure 2:

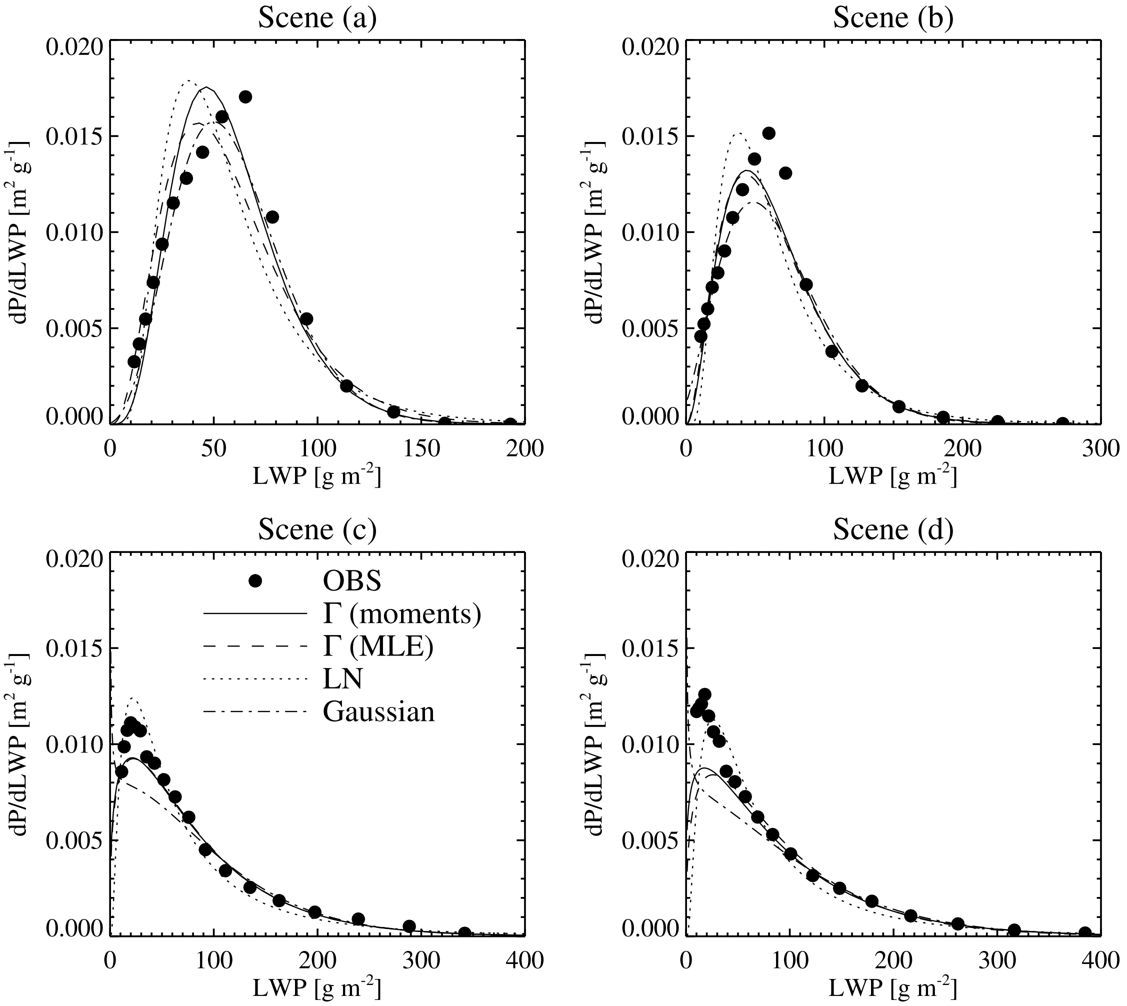
Scene (a)
Scene (b)
Scene (c)
Scene (d)
dP/dLWP [m² g⁻¹]
LWP [g m⁻²]
OBS
Γ (moments)
Γ (MLE)
LN
Gaussian
0.020
0.015
0.010
0.005
0.000
0
50
100
150
200
300
400

Figure 3:

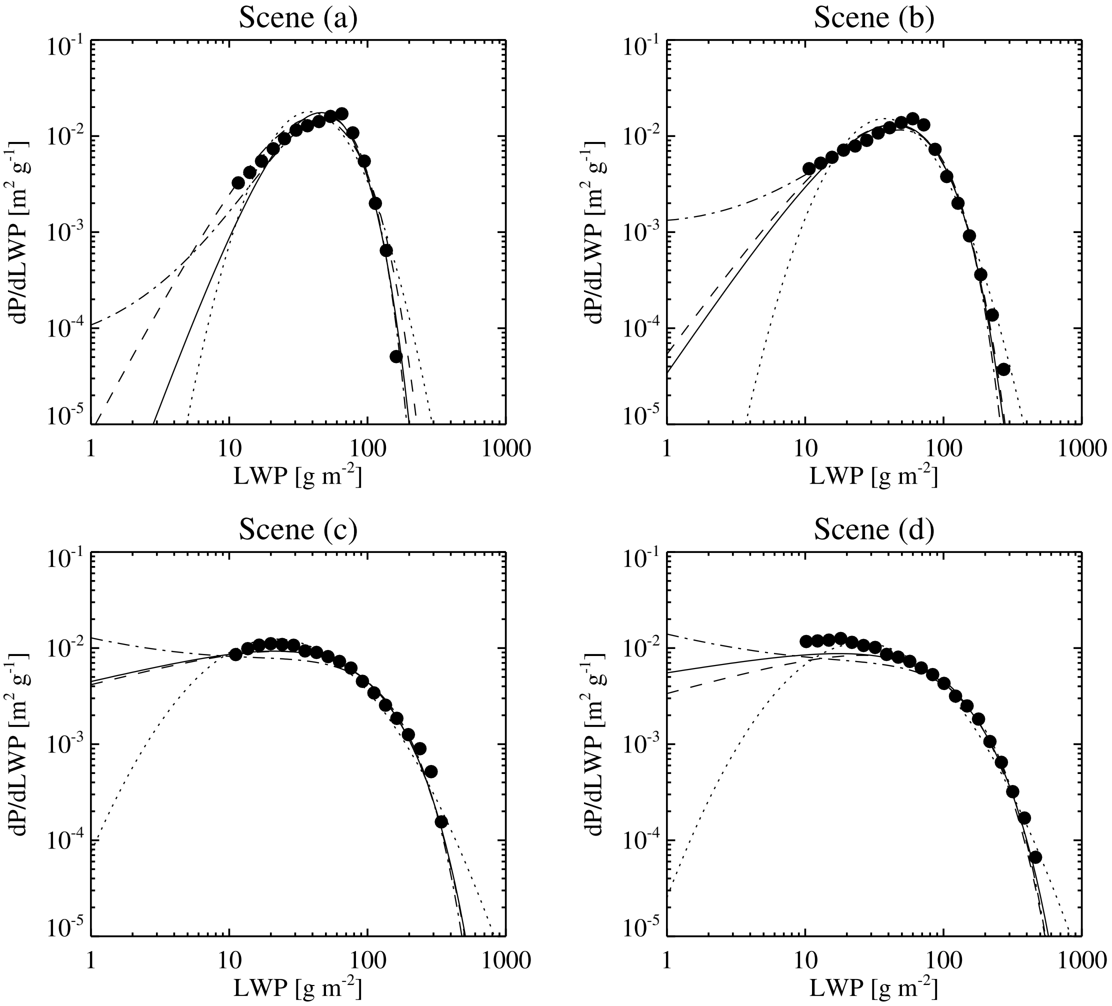
Scene (a)
Scene (b)
Scene (c)
Scene (d)
dP/dLWP [m2 g-1]
LWP [g m-2]
1
10
100
1000
10-1
10-2
10-3
10-4
10-5

Figure 3:

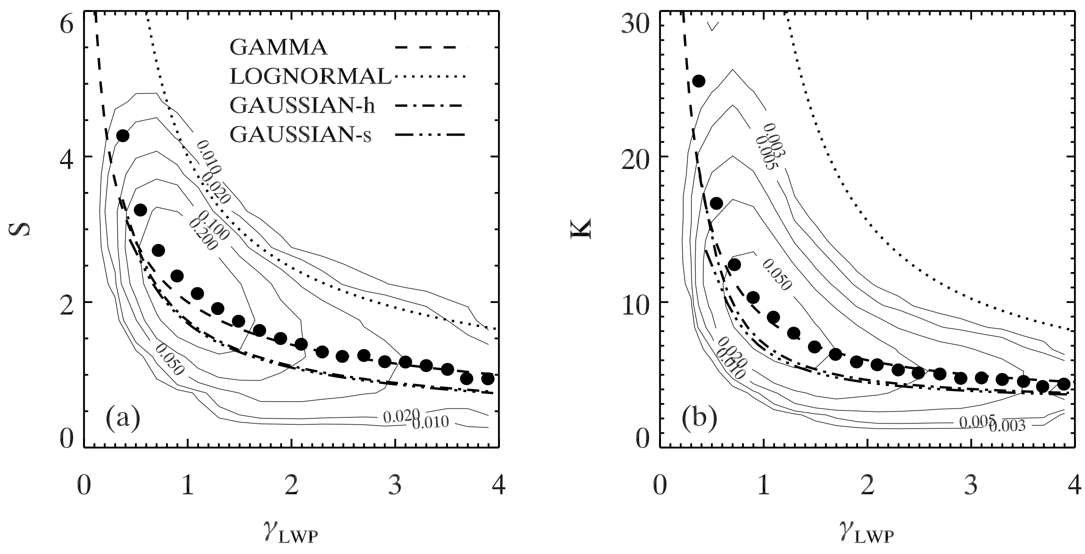
GAMMA
LOGNORMAL
GAUSSIAN-h
GAUSSIAN-s
(a)
(b)
S
K
γ_{LWP}
γ_{LWP}
0.010
0.020
0.100
0.200
0.050
0.003
0.005

Figure 4:

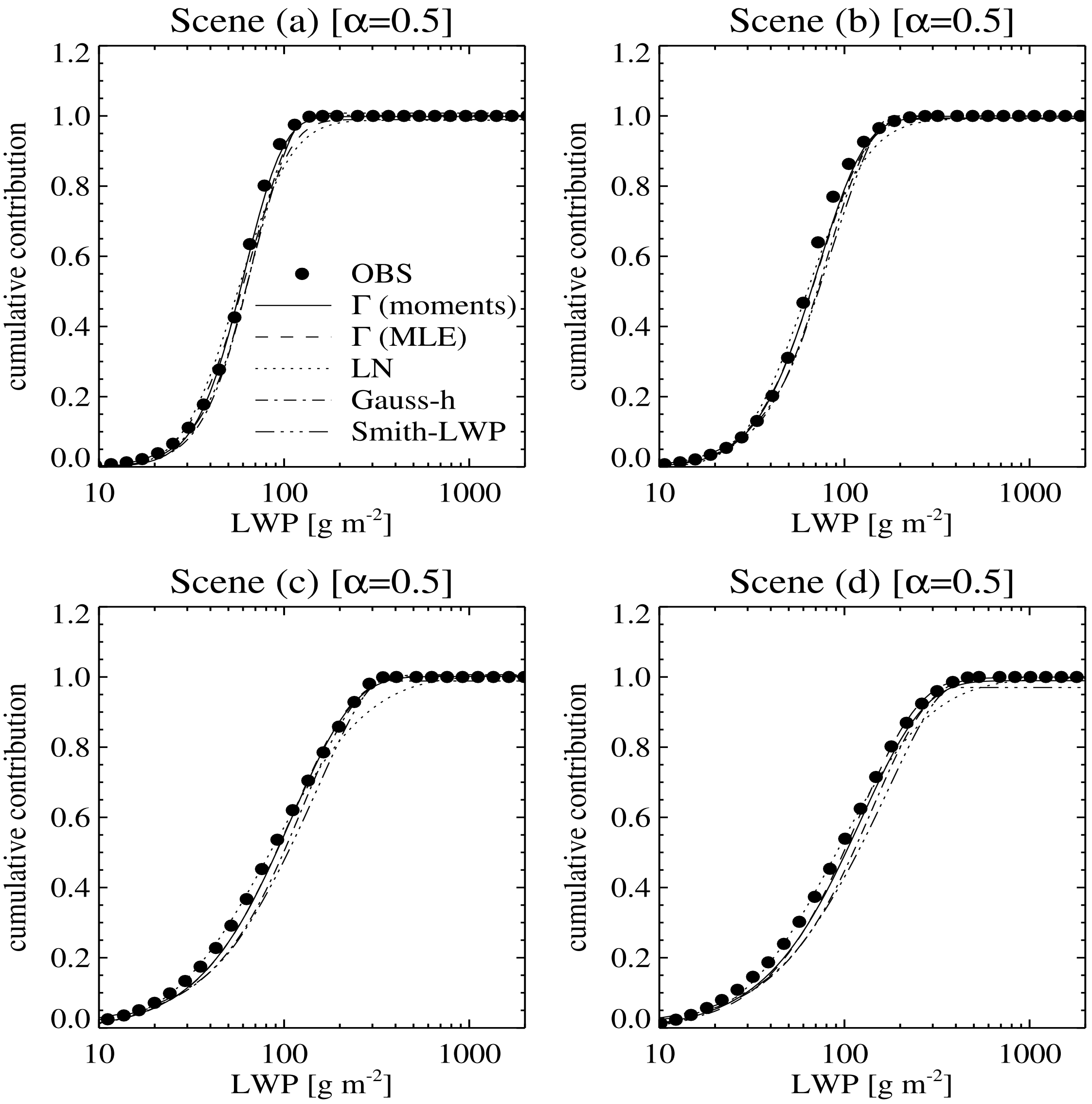

Scene (a) [α=0.5]
Scene (b) [α=0.5]
Scene (c) [α=0.5]
Scene (d) [α=0.5]
cumulative contribution
LWP [g m-2]
OBS
Γ (moments)
Γ (MLE)
LN
Gauss-h
Smith-LWP

Figure 5:

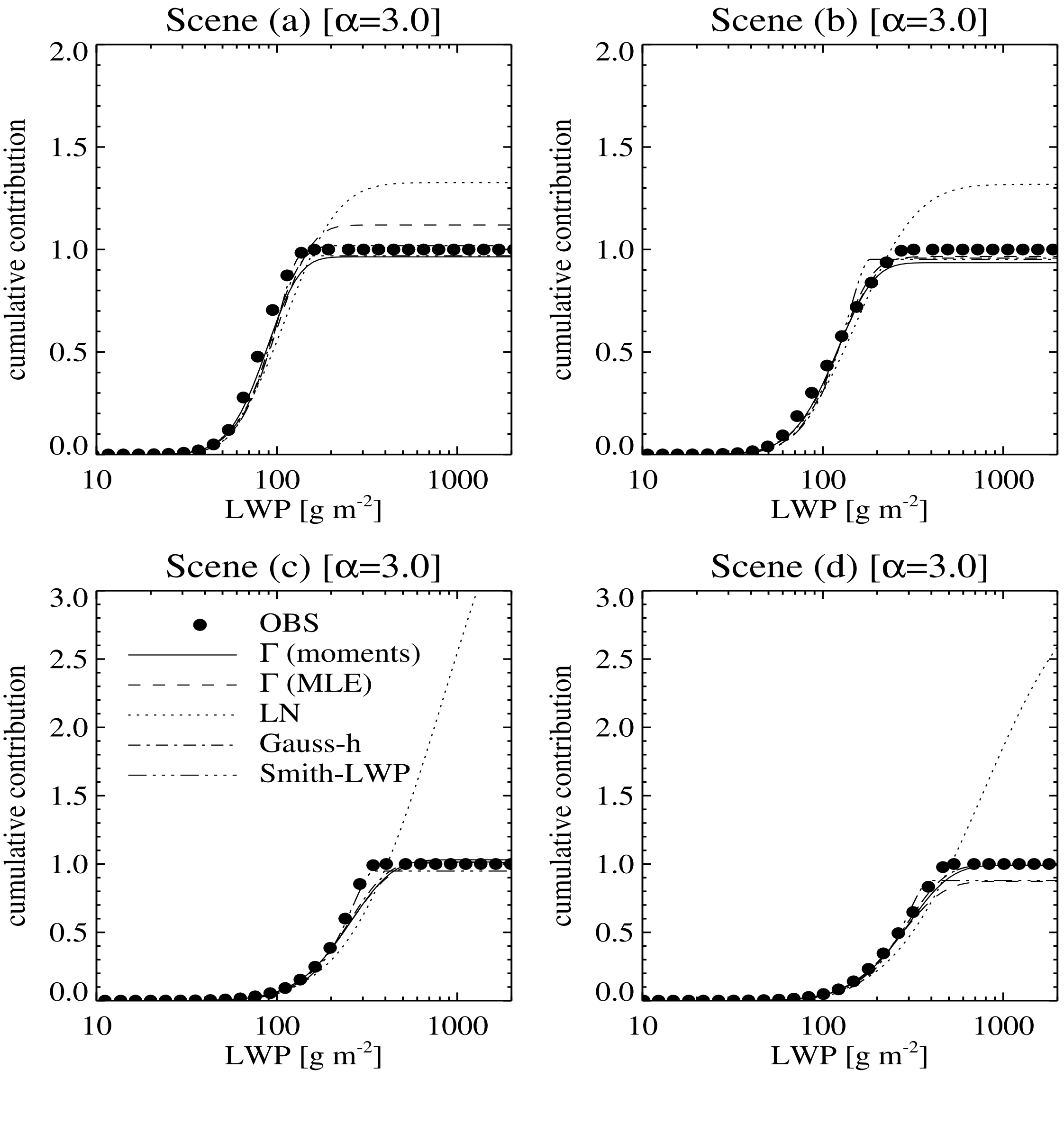
Scene (a) [α=3.0]
Scene (b) [α=3.0]
Scene (c) [α=3.0]
Scene (d) [α=3.0]
cumulative contribution
LWP [g m-2]
OBS
Γ (moments)
Γ (MLE)
LN
Gauss-h
Smith-LWP

Figure 6:

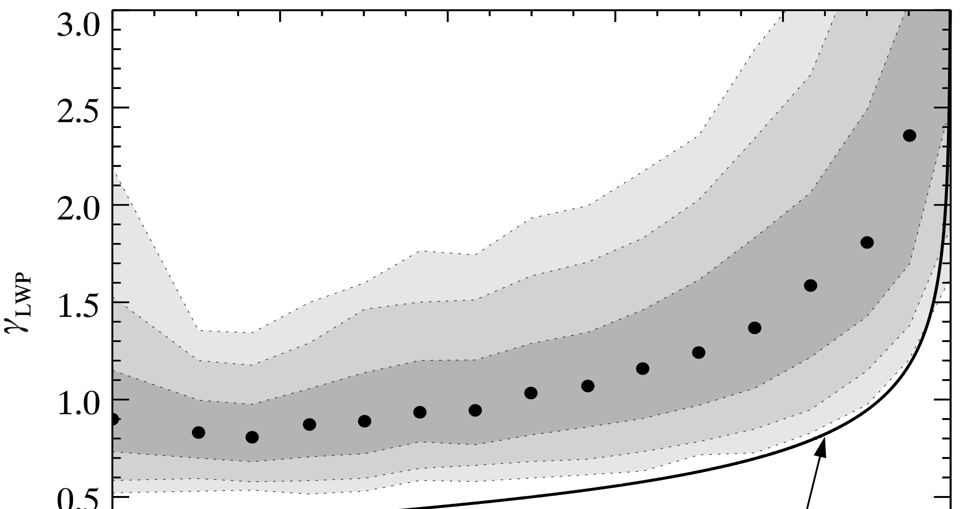

3.0
2.5
2.0
1.5
1.0
0.5
0.0
γ_{LWP}
Gaussian-h/Gaussian-s
0.0
0.2
0.4
0.6
0.8
1.0
CF

Figure 7:

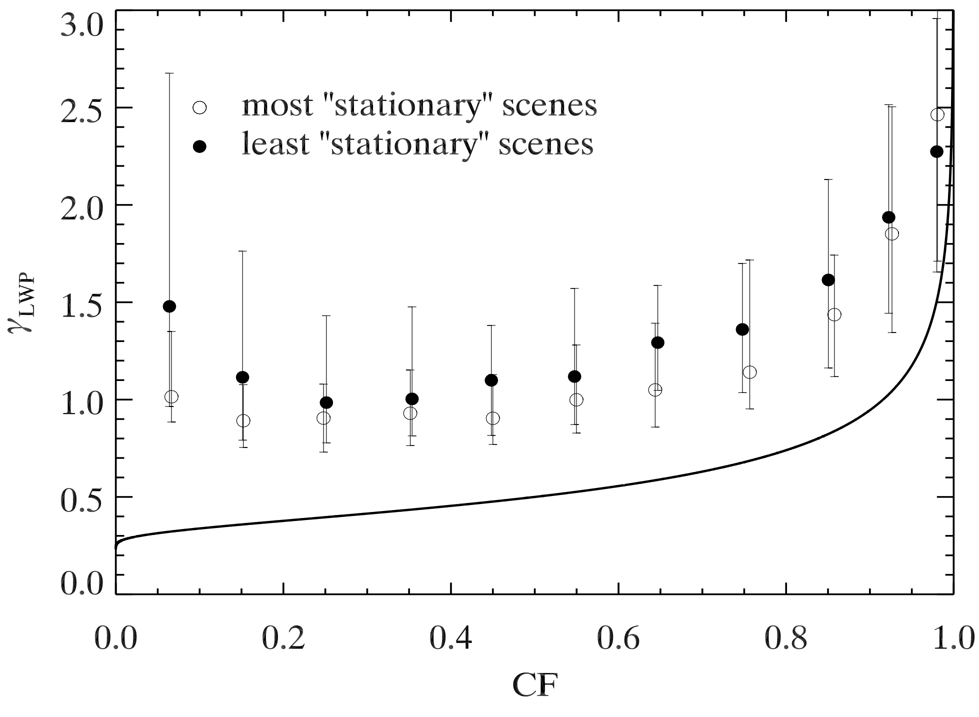

3.0
2.5
2.0
1.5
1.0
0.5
0.0
most "stationary" scenes
least "stationary" scenes
γ_{LWP}
0.0
0.2
0.4
0.6
0.8
1.0
CF

Figure 8:

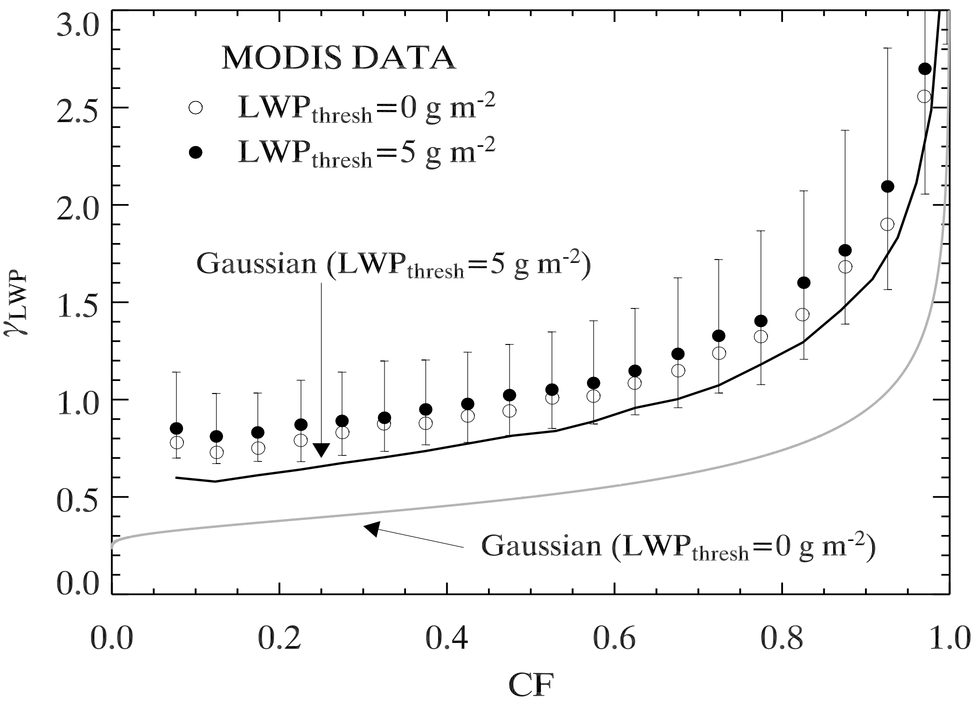
MODIS DATA
LWP$_{thresh}$=0 g m^{-2}
LWP$_{thresh}$=5 g m^{-2}
Gaussian (LWP$_{thresh}$=5 g m^{-2})
Gaussian (LWP$_{thresh}$=0 g m^{-2})
γ_{LWP}
CF
0.0
0.5
1.0
1.5
2.0
2.5
3.0
0.0
0.2
0.4
0.6
0.8
1.0

Figure 9:

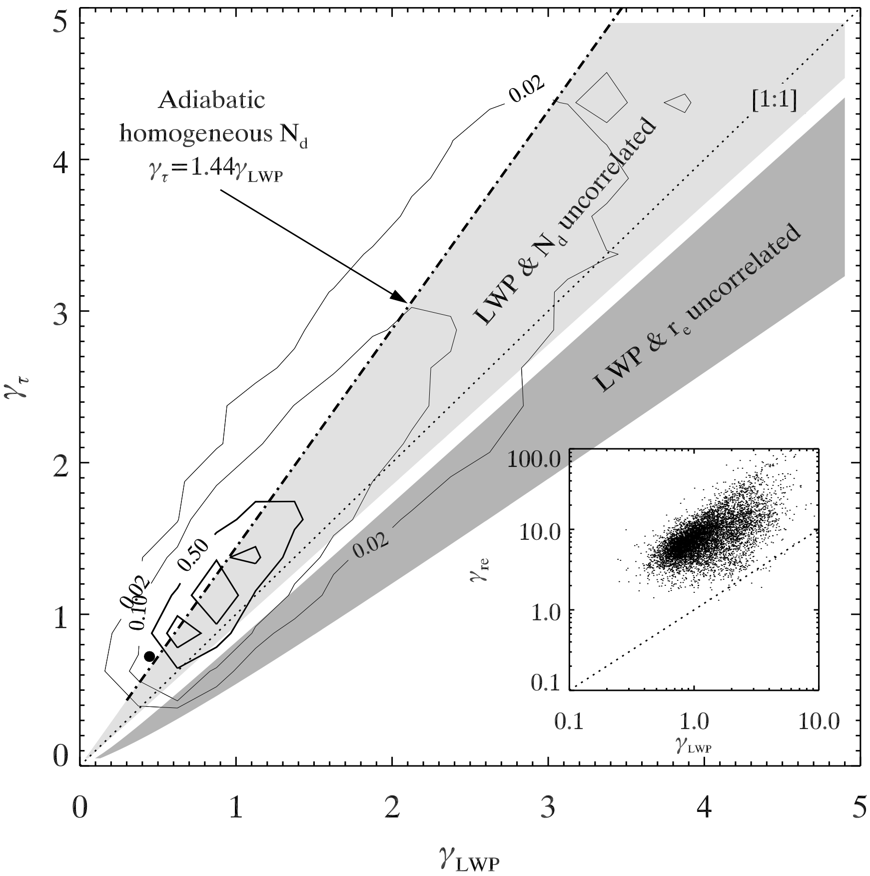
Adiabatic
homogeneous N_d
$\gamma_\tau = 1.44\gamma_{LWP}$
LWP & N_d uncorrelated
LWP & r_e uncorrelated
[1:1]
0.02
0.50
0.10
0.02
γ_τ
γ_{LWP}
γ_{re}
γ_{LWP}

Figure 10:

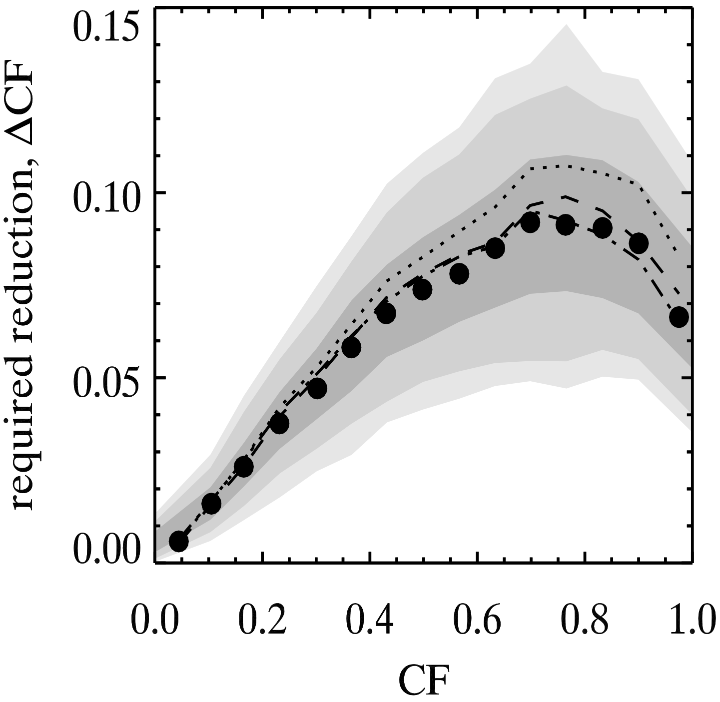

Figure 11:

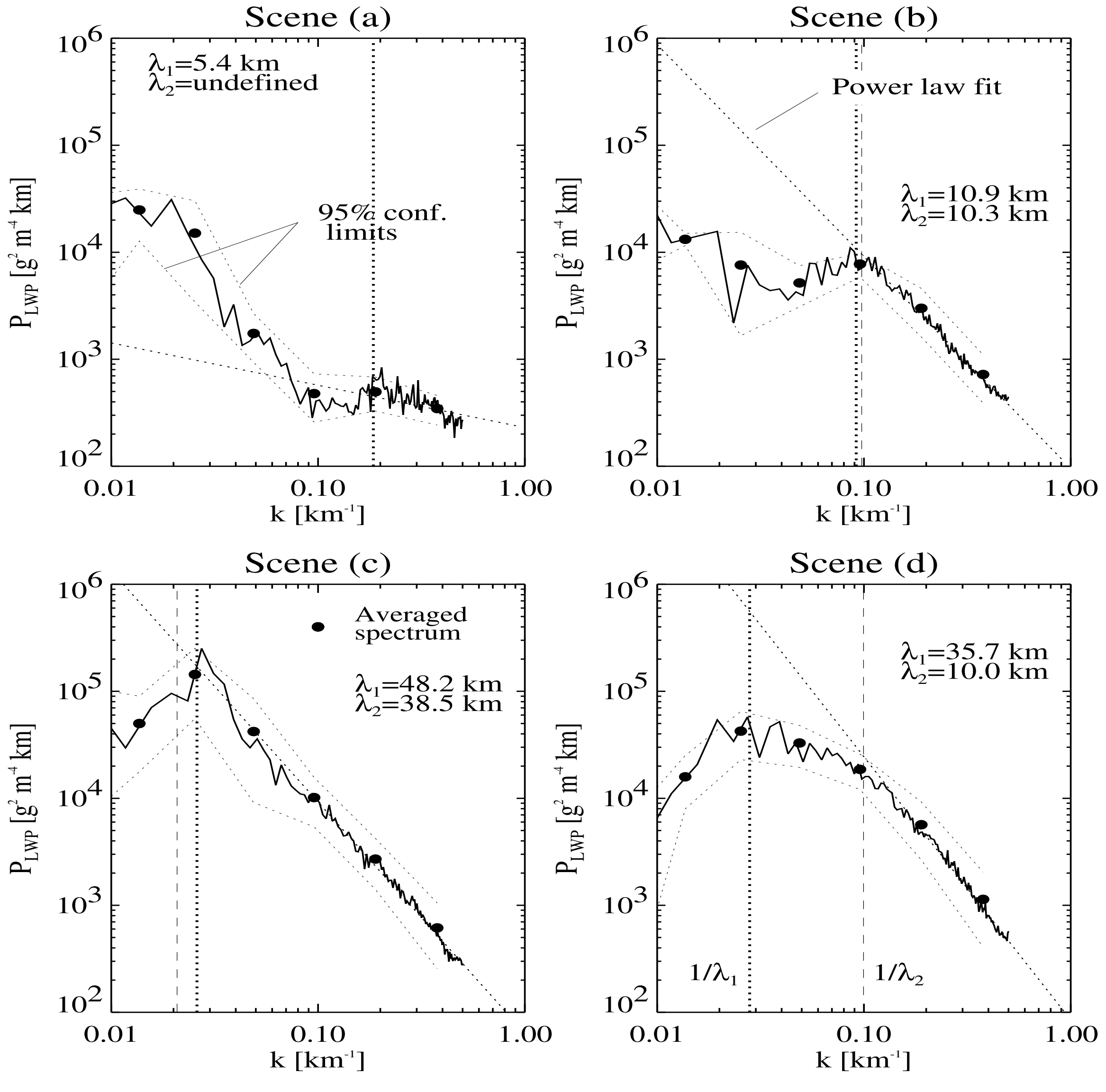

Scene (a)
λ_1=5.4 km
λ_2=undefined
95% conf. limits
Scene (b)
Power law fit
λ_1=10.9 km
λ_2=10.3 km
Scene (c)
Averaged spectrum
λ_1=48.2 km
λ_2=38.5 km
Scene (d)
λ_1=35.7 km
λ_2=10.0 km
$1/\lambda_1$
$1/\lambda_2$
P_{LWP} [g^2 m^{-4} km]
k [km^{-1}]

Figure 12:

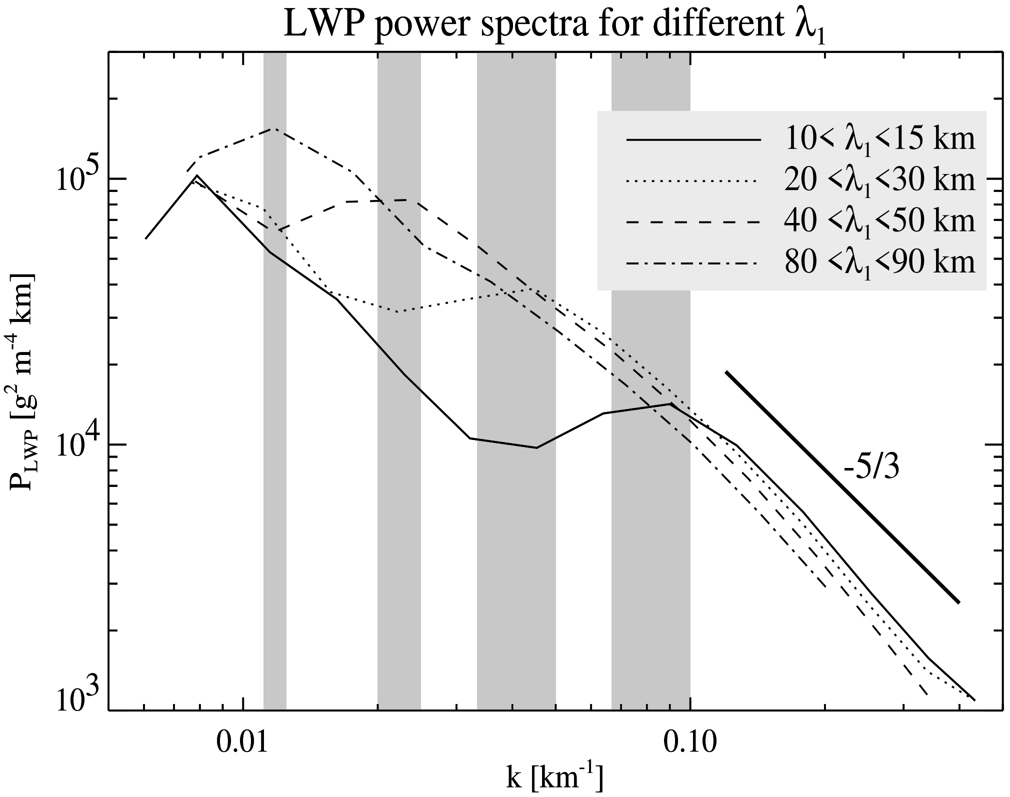
LWP power spectra for different λ_1
10^5
10^4
10^3
P_{LWP} [g^2 m^{-4} km]
0.01
0.10
k [km^{-1}]
10< λ_1<15 km
20 <λ_1<30 km
40 <λ_1<50 km
80 <λ_1<90 km
-5/3

Figure 13:

(a)

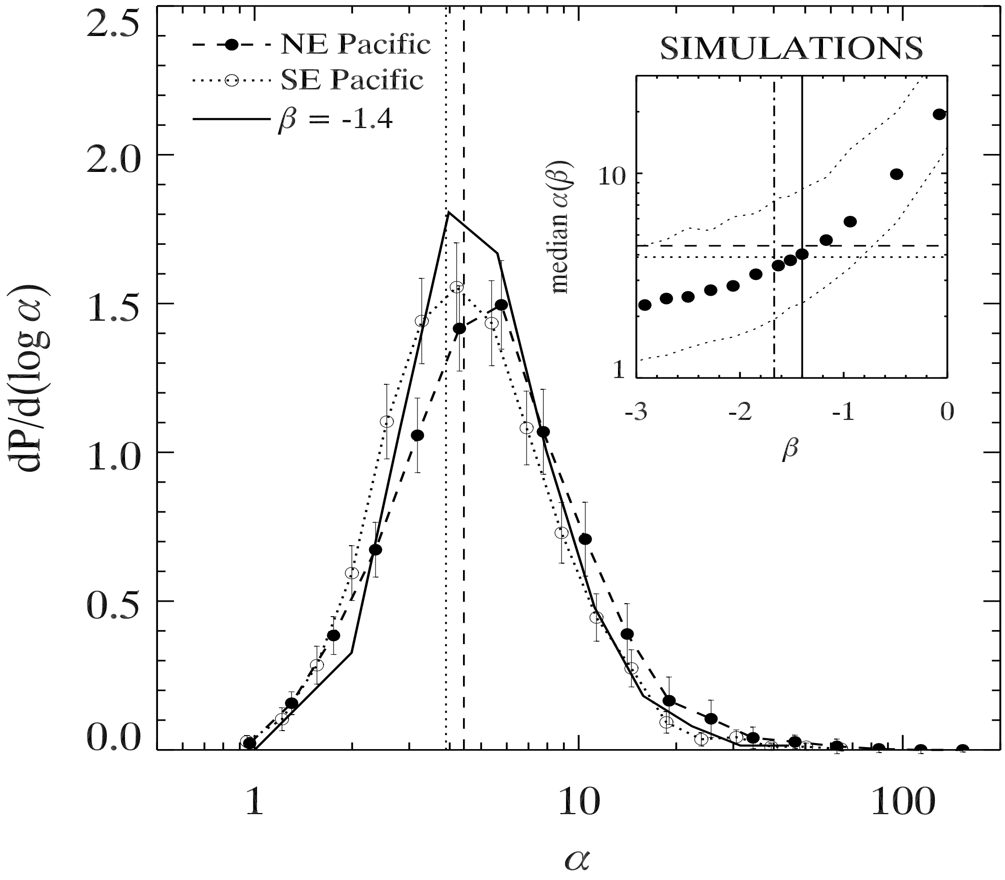

NE Pacific
SE Pacific
β = -1.4
SIMULATIONS
median $\alpha(\beta)$
β
dP/d(log α)
α

Figure 14: